UNITED NATIONS UNIVERSITY
UNU-GTP
Geothermal Training Programme

Orkustofnun, Grensasvegur 9,
IS-108 Reykjavik, Iceland

Reports 2019
Number 12

NUMERICAL MODELLING OF AHUACHAPÁN GEOTHERMAL FIELD, EL SALVADOR

José Erick Jiménez Majano
LaGeo S.A. de C.V.
15 Av. Sur, Col. Utila
Santa Tecla, La Libertad
EL SALVADOR
jjimenez@lageo.com.sv

ABSTRACT

A numerical model was developed for the Ahuachapán geothermal field, based on the last update of the conceptual model. The area under study is a volcanic geothermal system located in El Salvador that has been producing energy since 1975, with a current installed capacity of 95 MW_e and a total extraction flow of 890 kg/s. The main features of the conceptual model, such as upflow and outflow zones, barriers, depth of the reservoir as well as the lithologic column, were introduced into the model through a distribution of different rock properties and boundary conditions. For this study the TOUGH2 simulator was used for core calculations, along with python scripts to manage the data, create input files, and process the output. The mesh limits were established based on previous studies. The model is composed of 15 layers, each consisting of 3,020 elements. Pressure and temperature profiles were used to calibrate the natural state while 44 years of mass extraction and reinjection were introduced into the model to recreate how the reservoir conditions change throughout the utilization history. Flowing enthalpy of production wells and drawdown in monitoring wells were used as calibration data. An inverse modelling approach using iTOUGH2 was used to calibrate the permeability distribution and heat sources. Based on the good match of the natural state and the production history, a 20 years forecast was calculated assuming that the current conditions of exploitation will be maintained. The results show a drawdown of 1.5 bar in reservoir pressure, confirming the categorization of the field as an open system. The rock type distribution suggests that the horizontal permeability ranges from 15 to 160 mD and the vertical permeability ranges from 13 to 80 mD in the rocks below the wellfield.

1. INTRODUCTION

Geothermal resources are distributed all over the planet but are especially concentrated in volcanic regions where hot intrusions or magma act as a heat source and permeable fractures and faults control the flow pattern (Axelsson, 2012). The uses of geothermal energy range widely, from fish farming and district heating to power generation. These uses have a high impact on the surrounding communities and the global climate by reduction of CO_2 emissions.

The successful utilization of geothermal resources for long-term production includes the monitoring of

mass extraction, heat transport, pressure and chemical composition. This information allows an estimate of the equilibrium between utilization and renewability of the resource. In order to predict the future response of a geothermal system, several techniques have been applied, such as simple mathematical modelling, lumped parameter modelling and more detailed numerical modelling (Axelsson, 2012). Among these methods, numerical modelling has become a standard evaluation procedure of geothermal reservoirs (Pruess, 2002) including extensive models with tens of thousands of blocks (O'Sullivan et al., 2000) due to the increase in computational power. The core of these evaluations is based on the physics of the fluid flow and heat transfer based on the physical properties of the medium and the thermodynamic properties of the fluid. For this endeavour the first guide is the conceptual model of the system (Grant and Bixley, 2011) together with other data necessary to compare the initial state of the geothermal system and its response to exploitation.

For this study, a three-dimensional numerical model of the Ahuachapán geothermal field is developed based on the last update of the conceptual model. The major findings of the previous studies (Aunzo et al., 1989; ENEL-LaGeo, 2004) are presented. The iTOUGH2 simulator is used to perform calculations along with python and shell scripts to process the input data and the results from the modelling. Pressure and temperature logging, flowing enthalpy and drawdown data which are retrieved from the internal database of the operator of the geothermal field (LaGeo S.A. de C.V.) are used to calibrate and validate the model. The general approach presented by Bödvarsson and Whiterspoon (1989) is used. Thus, a natural state model is calibrated to estimate the initial conditions prior to the beginning of production. The aim of the model is, consequently, to predict the behaviour of the reservoir in terms of pressure drawdown and cooling effects while maintaining the current status of exploitation for the next 20 years.

2. AHUACHAPAN GEOTHERMAL FIELD

El Salvador is located on the Pacific Ocean coastline of Central America, on the Pacific margin of the Caribbean plate. The country is almost entirely underlain by Tertiary to Holocene rocks and debris. From south to north the country can be morphologically divided into five regions: coastal plains, costal ranges, Pacific volcanic chain, central graben and the northern mountain ranges (Laky et al., 1989).

The Ahuachapán geothermal field is a high-temperature geothermal field located 90 km west of the country's capital San Salvador. The geothermal field currently has 57 wells. The production wells range from a minimum of 590 m to maximum of 1645 m depth. The first well, AH-1, was drilled in 1968. The field started to generate electricity with a 30 MW_e unit in 1975. Currently, the installed capacity of 95 MW_e is supported by two single flash units and one double flash unit. Together with the Berlin geothermal field, another field under exploitation in El Salvador, geothermal electricity production in the country was 22.4% of the total production in July 2019 (Unidad de Transacciones S.A. de C.V., 2019). Figure 1 shows the well locations and status along with the main structures in the field.

2.1 Physical characteristics

2.1.1 Geological overview

The Ahuachapán geothermal field is located in the southern flank of the central graben and in the northwest sector of the Cerro Laguna Verde volcanic group (Cuellar et al., 1989). The volcanic activity of the region is related to the tectonic interaction in the subduction zone between the Cocos and Caribbean plates (Pedrazzi et al., 2019). The lithology is divided into the following four units: superficial materials, young agglomerates, Ahuachapán andesites and old agglomerates. The superficial materials are found in the top layer, ranging from 100 to 150 m depth, and contain a shallow aquifer which has unconfined characteristics and shows rapid response to changes in precipitation. The temperature in the aquifer under the wellfield ranges from 40 to 100 °C and increases from north to south. The second

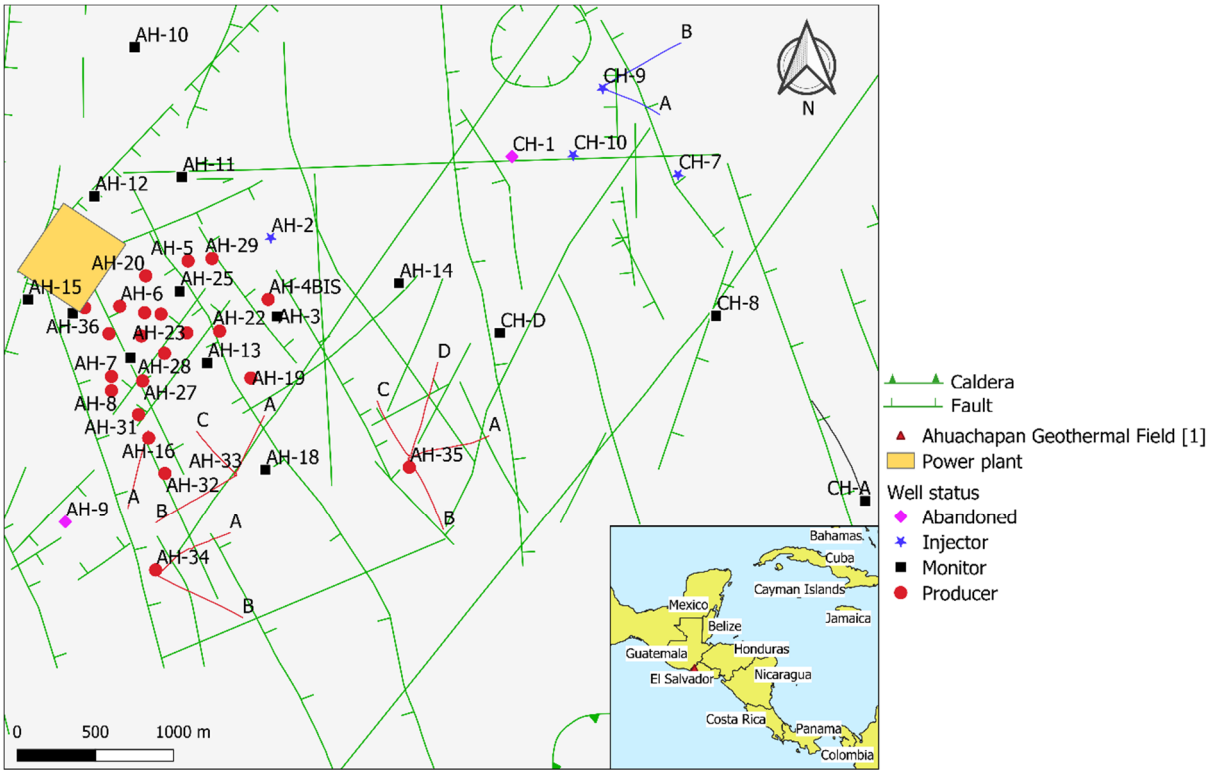

FIGURE 1: Ahuachapán geothermal field

lithological unit is a sequence of young pyroclastic and andesites rocks with a thickness of 300 to 800 m. The regional saturated aquifer is related with this structure. The Ahuachapán andesites are composed of highly fractured rocks and host the main geothermal reservoir. The thickness varies from 200 to 600 m. The fourth lithological structure consist of dense breccias, agglomerates and andesites (Laky et al., 1989).

The three main orientations of the fault systems are E-W (main central graben trend), NE-SW in the western sector of the field and NNW-SSE associated with surface hydrothermal activity (Monterrosa and Montalvo, 2010).

2.1.2 Geophysical overview

Different surveys have been carried out over an area of about 60 km^2. Results show low resistivity values (< 5 ohm-m) at depths of 500 to 1000 m. The low-resistivity values are associated with the geothermal reservoir (Santos, 2010). The transition of the system between the conductive to the lower resistivity layer is observed at 25 ohm-m (Monterrosa and Montalvo, 2010). The gravity data (Figure 2) shows that the production wellfield is located in the northern part of a gravimetric maximum with ENE-WSW trend and a secondary NNW-SSE trend is identified following the Chipilapa wells to the north (Santos and Rivas, 2009).

According to the surveys, the Ahuachapán and Chipilapa areas are parts of the same geothermal system. Therefore, a model with one geothermal system and a single heating location was proposed (ENEL-LaGeo, 2004). In this work, the results of the geophysical surveys are used to check the temperature distribution in the model and to establish the boundaries of the geothermal reservoir.

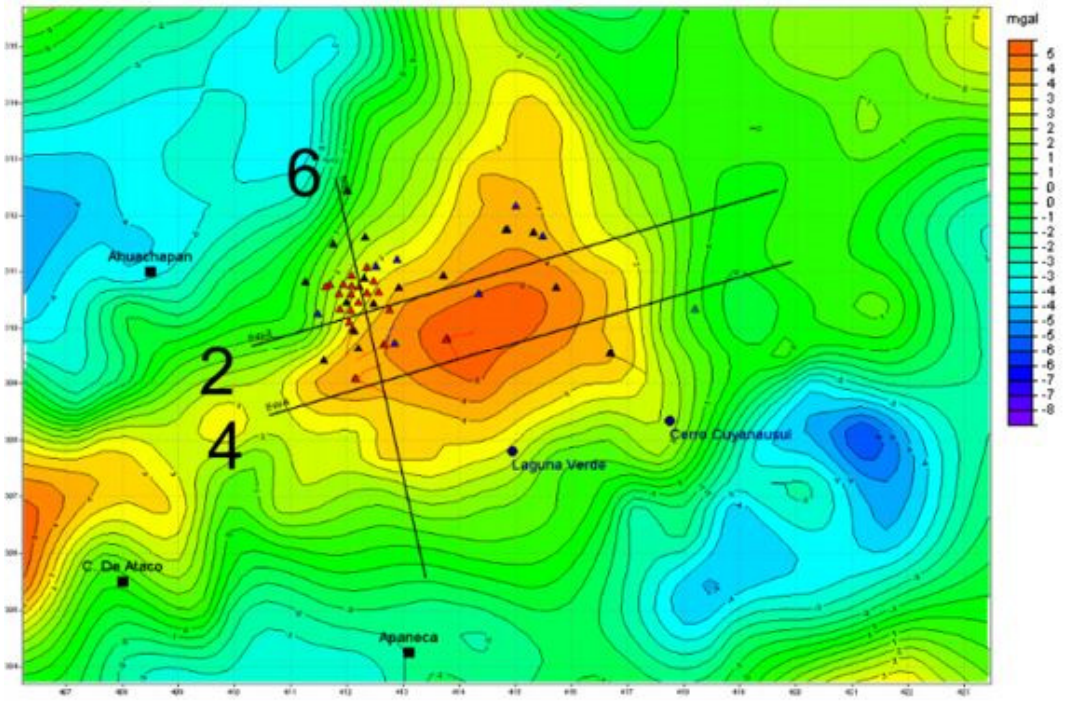

FIGURE 2: Bouguer 3° order residual map of the Ahuachapán geothermal area (ENEL, 2004)

2.1.3 Geochemical overview

Prior to exploitation, the three aquifers mentioned in the geological section were identified based on fluid chemistry, temperature and pressure response due to seasonal rainfall. The upflow zone is delimited by the increase of hydrogen content in the steam fumaroles toward the southeast suggesting the location at the north flank of the Laguna Verde volcano (Laky et al., 1989). The chloride distribution reveals an increasing temperature from 235 to 262°C from east to west due to the mixing with colder and lower salinity fluid from the east (Truesdell et al., 1989).

In response to pressure drawdown, high temperature reservoirs either boil or show dissolution processes. In this case, both physical processes are present but the main process seems to be boiling (Monterrosa and Montalvo, 2006). Figure 3 shows the increment of enthalpy as a boiling signal and a decrease in Cl as part of the dissolution process.

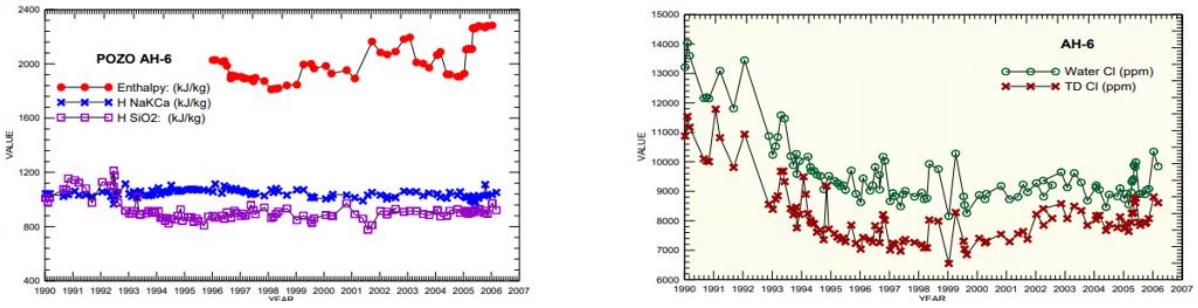

FIGURE 3: (a) Enthalpy evolution comparison and (b) Chloride history, both from well AH-6, from (Monterrosa and Montalvo, 2006)

Tracer tests

Tracer tests that have been carried out involving wells AH-2, AH-5, AH-29, AH-32 and AH-18 reveal that the fluid moves from the southern part through the centre of the field at lower velocities than from

the north to the centre (Montalvo, 1996). Thus, the connection between the wells and the hot recharging region in the north is confirmed.

For this study, the northeast part of the field is considered a cold zone and the southwest part an outflow zone underneath which the heat source is located.

2.1.4 Formation temperatures

The pressure and temperature logs of the wells were recorded under different conditions: dynamic flowing, thermal recovery, shut-in, bleeding, etc. Unfortunately, the recovery data is not sufficient to apply the Horner method to estimate the formation temperature. However, all the wells were logged several times during shut-in or bleeding conditions before the production started or during unit maintenance. For this study one of these logging results was selected as the formation temperature for each well included in the model.

In some of the wells the pressure was not measured at the same time. In such cases the temperature profile is used to calculate the downhole pressure profile, assuming a hydrostatic column and saturation conditions. The water level is based on other pressure profiles while projecting the trend to the vertical axis. Appendix I shows the rock distribution in the different layers of the model, while a detailed view of all the loggings is shown in Appendix II where they are compared to calculated values of the natural state model.

Figure 4 shows a horizontal cross-section at 0 m a.s.l. of the formation temperature. The values increase from north to south and from east to west. The temperature front is traveling from SSW to NNE in the production field and the reinjection field shows the lowest temperature.

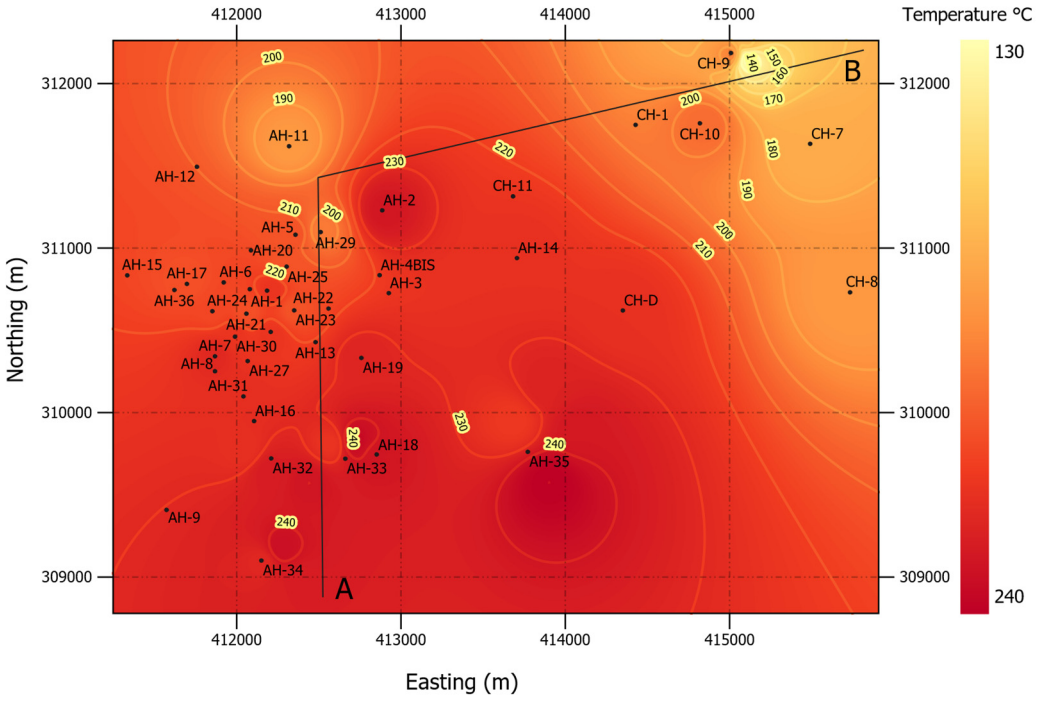

FIGURE 4: Contour plot of temperature distribution at 0 m a.s.l.

Interpreted stratigraphy data were collected for all the wells in the field and integrated with the formation temperature, well geometry and topography using Leapfrog Geothermal (Leapfrog, 2019). Thus, from the identified stratigraphy units and formation temperature distribution a better permeability distribution can be made for the numerical model. The vertical cross-section shown in Figure 5 presents the

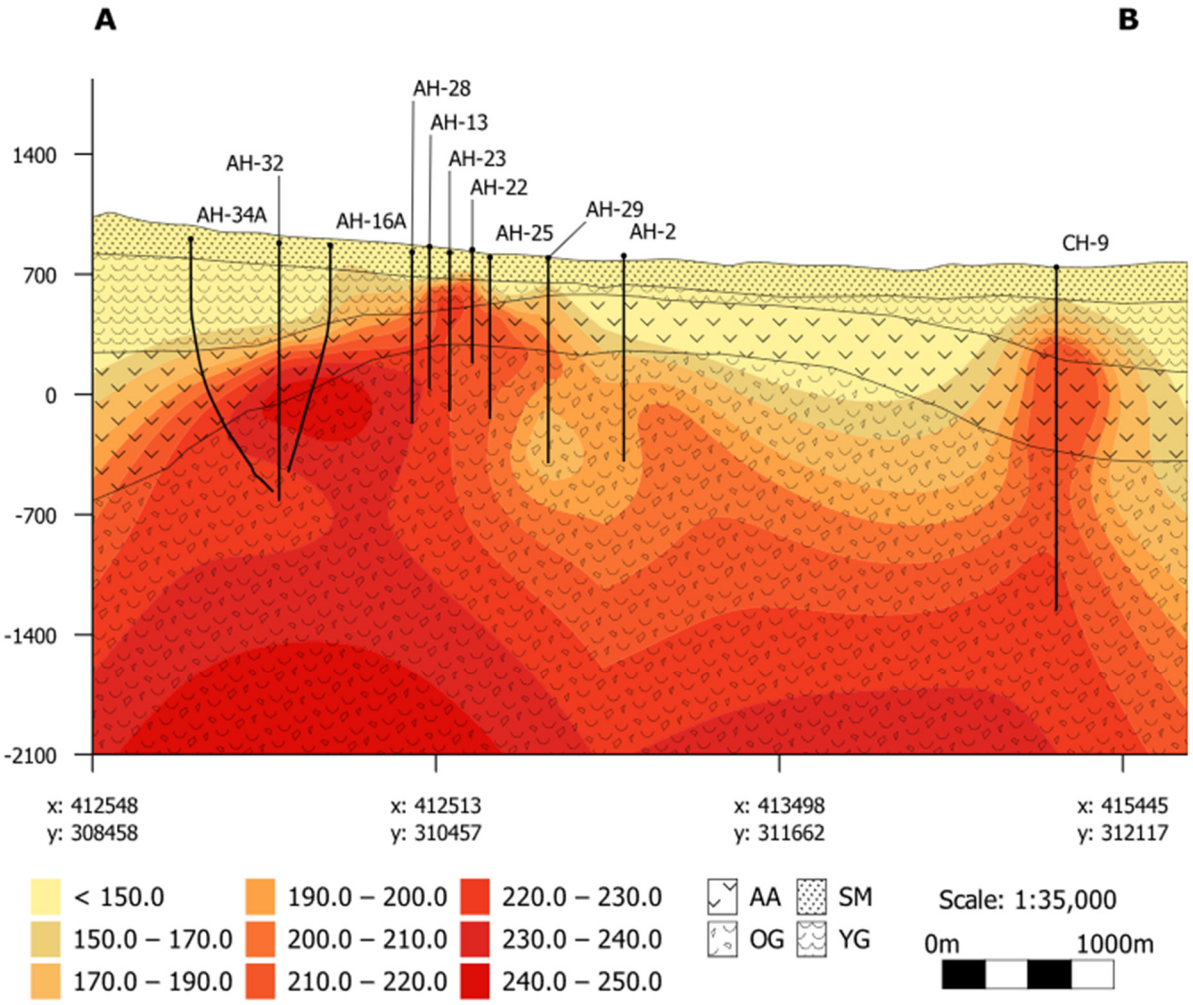

FIGURE 5: Vertical cross-section A-B (from Figure 4) of formation temperature distribution, showing the lithologic column in the background. SM stands for superficial materials, YG for young agglomerates, AA for Ahuachapán andesites and OG for old agglomerates

formation temperature distribution with the lithologic column in the background, no fractures or faults are shown. The high temperature (more than 200°C) follows the Ahuachapán andesites distribution. Therefore, the higher temperature is shallow in the main production field and it moves deeper to the south as the lithologic column moves. Between wells AH-2 and CH-9, low values of temperature can be found, representing the connection between Ahuachapán and Chipilapa.

2.2 Conceptual model

Surface manifestations are spread over 100 km^2 and can be divided into high temperature fumaroles, steaming ground on the northern slopes of Laguna Verde, and hot springs north of the geothermal area. The chemical analyses of the fumaroles show similar composition indicating a common source. The natural discharge of the system is located north of a hot spring area called El Salitre, which prior to exploitation showed a higher chloride concentration explained by the direct connection with the reservoir. During exploitation the flow rate has decreased and its salinity has been reduced. In the upflow zone temperatures are above 250°C, as the chemical analysis and temperature distribution reveal. The regional saturated aquifer mentioned before has a higher pressure than the underlying geothermal reservoir and in most of the area is separated from the hot reservoir by a low permeability layer. However, in the eastern part of the field, there is a hydrological communication with the geothermal reservoir trough faults and fractures allowing downward flow of liquid from the aquifer. The extent of

the reservoir is limited in the north and in the west by a barrier that might be associated with fault structures. The presence of these barriers can be inferred from the rapid temperature drop demonstrated by logs from wells AH-10, AH-8, AH-9 and AH-15 (Aunzo et al., 1989). Figure 6 shows the hydraulic connection and the main pattern of the convection cell between the production and reinjection field.

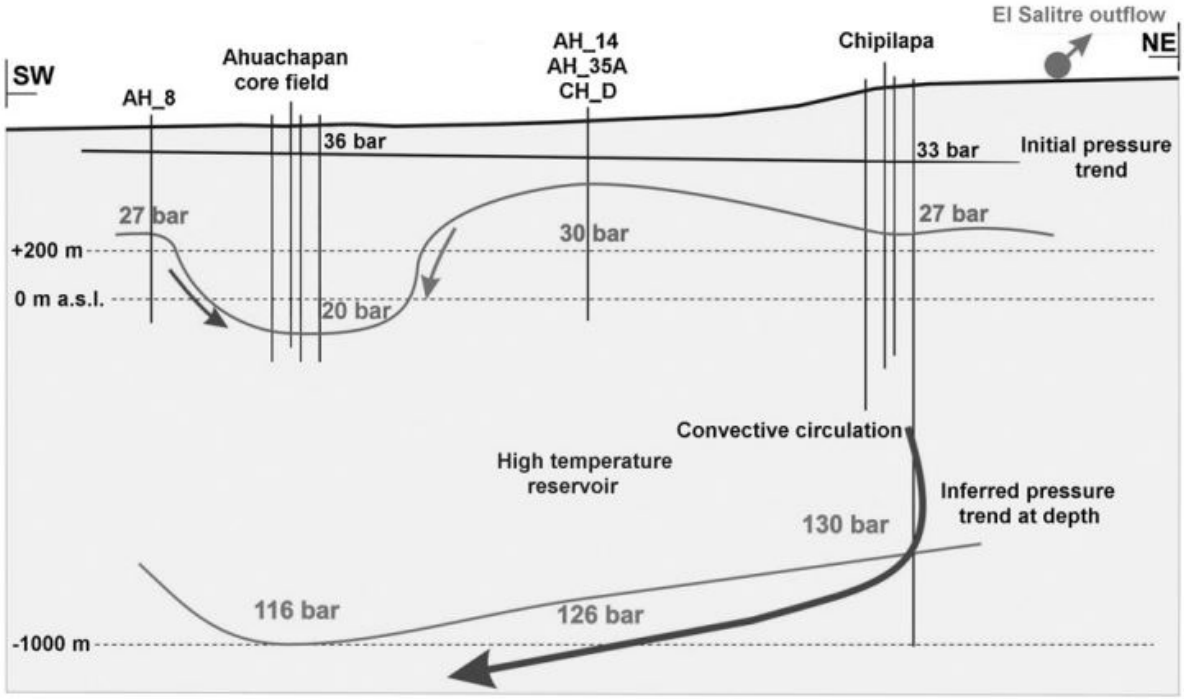

FIGURE 6: Cross-section of the conceptual model (From ENEL-LaGeo, 2004)

The main reservoir depth ranges from 900 to 1200 m with measured temperature from 230 to 250°C. Nevertheless, the centre of the field is shallow and is in a range of 500-800 m depth. The chemical history indicates that the reservoir has been diluted by less than 20% (Monterrosa and Montalvo, 2010).

2.3 Data sources

Data have been collected since the first well was drilled. Nowadays, the field data are systematically stored in a PostgreSQL database called GMS (LaGeo, 2019) and can be accessed through the intranet of LaGeo. This database includes information such as:

- Temperature and pressure logs
- Well tracks
- Production history of each well
- Production curves
- Injection test data
- Pressure drawdown

Most of the data that is needed in this study to calibrate the model and to establish proper boundary conditions are extracted from the GMS database. The scripts described in later sections are developed to connect and extract the data from this database.

3. DISTRIBUTED PARAMETER MODEL

3.1 Numerical modelling background

In the geothermal industry, numerical methods are used to model the behaviour of geothermal reservoirs. For this study TOUGH2 was used. This simulator is a general-purpose numerical simulation program for multidimensional mass and heat flow for multicomponent and multiphase fluids in porous and fractured media (Pruess et al., 1999). Through the solution of the general energy and mass equation based on a given geometry, fluid properties and rock distribution, the simulator is capable of reproducing the reservoir conditions to forecast the response of current or future scenarios as well as to confirm the nature of the system.

3.1.1 Mathematical theory

The general mass and energy balance equation used by TOUGH2 is:

$$\frac{d}{dt}\int_{V_n} M^{\kappa} dV_n = \int_{\Gamma_n} \boldsymbol{F}^{\kappa} \cdot \boldsymbol{n} d\Gamma_n + \int_{V_n} q^{\kappa} dV_n \tag{1}$$

where V_n = Arbitrary volume;
M = Mass or energy per volume;
κ = Mass or energy component;
F = Mass or energy flux;
q = Sinks and sources;
Γ_n = Closed surface;
$\boldsymbol{n}$ = Normal vector on the surface of element $d\Gamma_n$.

The mass accumulation term is:

$$M^{k} = \phi \sum_{\beta} S_{\beta} \rho_{\beta} X_{\beta}^{\kappa} \tag{2}$$

where β = Fluid phase;
ϕ = Porosity;
S_{β} = Saturation of phase β;
ρ_{β} = Density of phase β;
X_{β}^{κ} = Mass fraction of component κ present in phase β.

The heat accumulation term for a multiphase system is:

$$M^{NK+1} = (1-\phi)\rho_R C_R T + \phi \sum_{\beta} S_{\beta} \rho_{\beta} u_{\beta} \tag{3}$$

where $NK+1$ = Heat component;
ρ_R = Rock density;
C_R = Rock specific heat;
ρ_{β} = Density of phase β;
T = Temperature;
u_{β} = Internal energy in phase β.

The advective mass flux in Equation 1 is described by:

$$\boldsymbol{F}^{\kappa}|_{adv} = \sum_{\beta} X_{\beta}^{\kappa} \boldsymbol{F}_{\beta} \tag{4}$$

where, the individual fluxes are given by a multiphase version of Darcy's Law:

$$\boldsymbol{F}_\beta = -k\frac{k_{r\beta}\rho_\beta}{\mu_\beta}(\nabla P_\beta - \rho \boldsymbol{g}) \tag{5}$$

where k = Absolute permeability;
$k_{r\beta}$ = Relative permeability in phase β;
ρ_β = Density of phase β;
μ_β = Viscosity in phase β;
$\boldsymbol{g}$ = Gravity;
P_β = Fluid pressure in phase β, which is a sum of the pressure and the capillary pressure.

3.1.2 Numerical theory

In order to solve the equations listed above, space and time are discretized to solve the equations by the integral finite difference method. Basically, integrals are approximated as a discrete sum of the values involved (Pruess et al., 1999). For instance, the first element on the right in equation (1) is written as in (6). The discretization approach used in this method and the definition of the geometric parameters are shown in Figure 7.

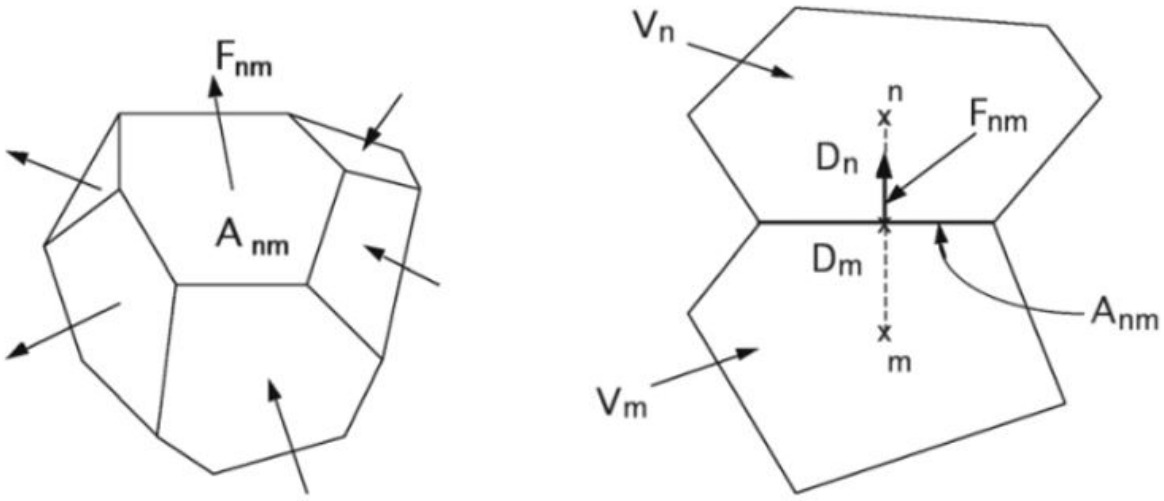

FIGURE 7: Space discretisation and geometry (Pruess et al., 1999)

$$\int_{V_n} \boldsymbol{F}^\kappa \cdot \boldsymbol{n} d\Gamma_n = \sum_m A_{nm}F_{nm} \tag{6}$$

where F_{nm} = Average value of normal component of F over the surface;
A_{nm} = Normal surface;
n = Index for the volume n;
m = Index for the volume m.

3.1.3 Inverse modelling

iTOUGH2 is a simulation-optimization framework for the TOUGH2 program (Finsterle, 2015). It supports three application modes:

1. Sensitivity analysis: identify the most sensitive parameter related with the model output. Furthermore, it helps to detect parameter combination that creates similar system behaviour.

2. Parameter estimation (inverse modelling): calculate the required parameter for a set of calibration points.
3. Uncertainty propagation analysis: the forecast quality of a given model is studied through the impact of parameter uncertainties.

The parameter estimation mode is described in detail in this section. A parameter vector **p** of length *n* containing the input parameters is given and an observation vector **z** of length *m* containing the calibration points at discrete points in space and time. The differences between the measured and calculated system are summarized in the residual vector **r** of length *m*. iTOUGH2 performs a simulation based on updates of the vector **p**. The increase or decrease of a parameter depends on the value of the objective function (S_{obj}) which is a norm of the weighted residuals. Therefore, the minimization algorithm looks for a minimum value for the n-dimensional objective function. The minimization procedure is finished once the objective function is not decreasing further. A representation of the objective function in a two-dimensional space is shown in Figure 8a. The Levenberg-Marquardt method (Figure 8b) is used as minimization algorithm in this study. For this method two parameters are defined: λ_{Lev} (Levenberg parameter) and ν_{Marq} (Marquardt parameter). The Levenberg parameter describes the steps along the gradient of the objective function (S_{obj}) and the inverse of the Marquardt parameter is used to decrease λ_{Lev} after a successful step (Finsterle, 2007). Depending on the quantity of parameters selected the procedure can in some cases reach a local minimum rather than a global minimum.

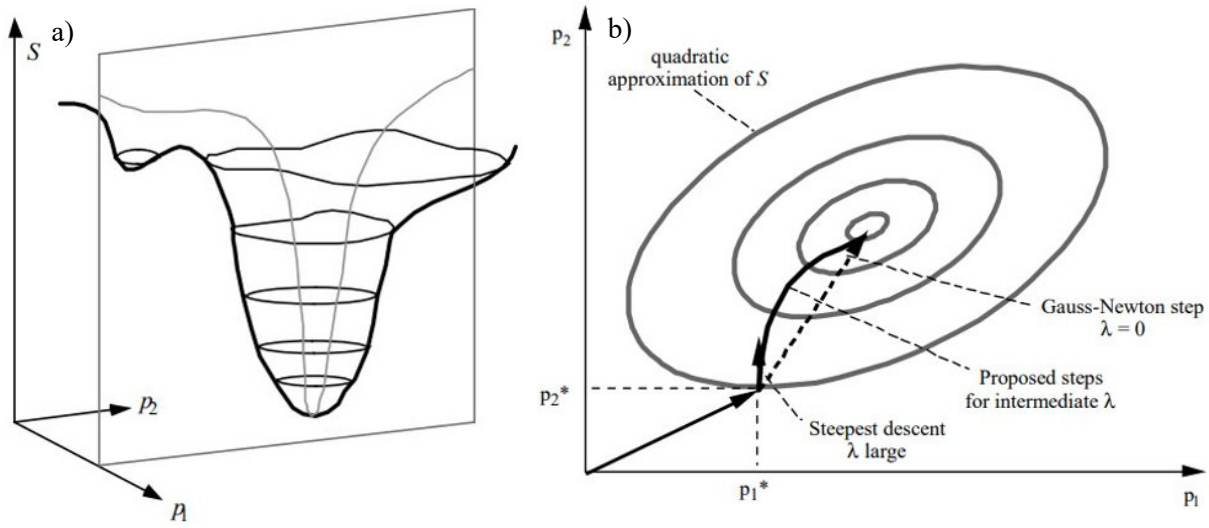

FIGURE 8: (a) Objective function (S_{obj}) in two-dimensional space. (b) Steps proposed by the Levenberg-Marquardt method from Finsterle (2007)

For this study iTOUGH2 is used to control the general behaviour of TOUGH2 and to perform an inverse modelling after a manual trial and error procedure.

3.2 Model setting

For this study several preprocessor and postprocessor scripts were written using the programming language Python (Python Software Foundation, 2019) to generate the mesh, establish the initial conditions of the top layer, generate input files and plot the required output. Steinar (Vatnaskil Consulting Engineers, 2015) was used to set the rock distribution throughout the layers and to establish the initial pressure and temperature for every element. Figure 9 shows the main process in terms of steps, scripts, and programs.

3.2.1 Preprocessor

The main preprocessor script is pyamesh which creates a mesh using the Voronoi principle used in AMESH (Haukwa, 1998). AMESH generates discrete grids for numerical modelling and transportation problems where the main objective is to use the finite volume method. Pyamesh creates three different zones: the outer mesh, the inner mesh and the wellfield. For the outer and inner mesh, a space between the elements is needed as well as the limits of each one, the outer mesh consists of square elements and the inner mesh of hexagonal elements. For the wellfield the wells coordinates are required. Therefore, the program creates irregular elements based on an established radial distance criterion.

The other python scripts mentioned in Figure 9 create the GENER block for the forward run and the OBSERVATION block for the inverse run by processing data retrieved from the database maintained by LaGeo. Table 1 shows the description, the purpose and the required input and output of each of the scripts.

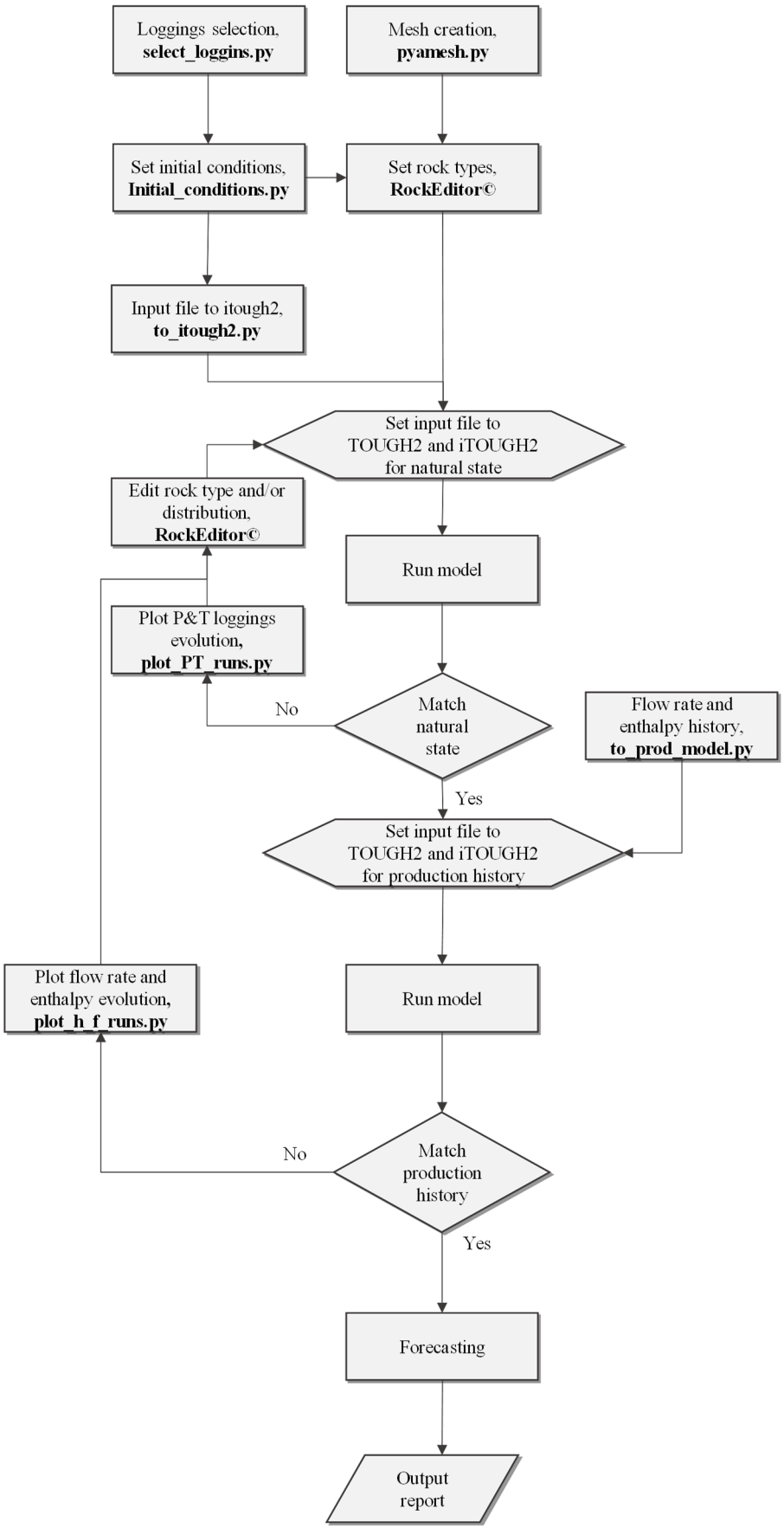

FIGURE 9: Flow chart, scripts for mesh creation and pre/post processing

TABLE 1: Description of python scripts

Script name: purpose	Input	Output
pyamesh.py: generate an irregular mesh with n layers	- X and Y location for the wells - X and Y mesh limits - X and Y elements distance from the border to outer mesh - X and Y elements distance for the inner mesh - Radius criteria, minimum distance between centres - Elevation value for the top layer - Layers thickness	- ELEME, CONNE, in and segmt files - Optional: mesh plot and shapefile of selected layer
selected_loggins.py: establish pressure and temperature along well track	- Well name and id or date of selected logging	- X, Y, Z, T and P for every well in a text file for the selected logging - Generated input files for temperature and pressure used for Leapfrog Geothermal
initial conditions.py: establish pressure and temperature for all the elements in the top and bottom layer of mesh	- Temperature and pressure for the outer mesh in the top and bottom layer	- INCON file for the elements at the top and bottom layer
to_itough2.py: generate the required conditions for every element along the well track in terms of pressure and temperature	- Logging for each selected well	- Text file to be append to the main iTOUGH2 input file
plot_PT_runs.py: compare results of P&T profiles for each well after each run	- P&T for each block in the well track	- PDF file with figures comparing the measured P&T logging, the results of the previous and current TOUGH2 run and rocks parameters of the current run
to_prod_model.py: generate the necessary input data for the production matching	- List of selected wells - Initial and final date of the production period	- Text file to be append to the main iTOUGH2 input file - Text file to be append to the main TOUGH2 input file
plot_h_f_runs.py: compare the values of flowing enthalpy and flow mass after each run	- Flowing enthalpy and mass flow for every selected well (database)	- PDF file with plots comparing the measured flowing enthalpy and mass flow with the results of the previous and current TOUGH2 run and rocks parameters of the current run
geometric_functions.py: transform measured depth to true vertical depth values, extract values of P&T at different depth, generate pressure profile base on a temperature logging assuming saturation conditions and water level projection based on static pressure logging	- Depending on selected function: well name, logging either pressure or tempera-ture, true vertical depth point or measured depth point	- Depending on selected function: variable value a long geometry of the well, pressure profile and water level depth. Conversion from measured depth to true vertical depth

3.2.2 Postprocessor

Several simple shell scripts are used to extract the data after each run. With a python script the data is plotted on a single chart to observe the evolution of the model (python scripts are described in Table 1).

3.3 Numerical model

3.3.1 Mesh

In order to obtain accurate results, grid blocks should be chosen sufficiently small so the variation of thermodynamic conditions between grid blocks is modest. This is especially important near the production wells, injection wells and in the upflow and recharge areas. However, it is also desirable to have a large model domain so that the fluid supply to the wells is controlled by the model rather than by artificial boundaries (Pruess, 2002).

In the present work, the boundaries that are used are based on a previous model developed by LaGeo (LaGeo, 2010). These limits, in NAD27 coordinates, are 404,000 to 424,000 from west to east and 302,000 to 322,000 from south to north. The mesh (Figure 10a) consists of 15 layers that are shown in Figure 10b. There are 3020 elements per layer and 45,300 elements in total. The height of the model volume is 2700 m. The smaller elements at the centre allow to better describe the structures incorporated in the conceptual model such as barriers, high permeability areas and rock type distribution based on lithology. The most important features of the mesh are listed below:

- The name of the elements starts with a letter from A (top) to O (bottom).
- No block is closer than 150 m to the wells unless it is another well.
- The elevation of the top layer is 600 m a.s.l.
- In the far-field, the space between the elements is 1000 m in X and Y direction and the elements are of rectangular shape. The distribution starts 1000 m from the boundaries of the mesh.
- For the wellfield, the distance between the elements is 125 m and the elements in the mesh are hexagonal.

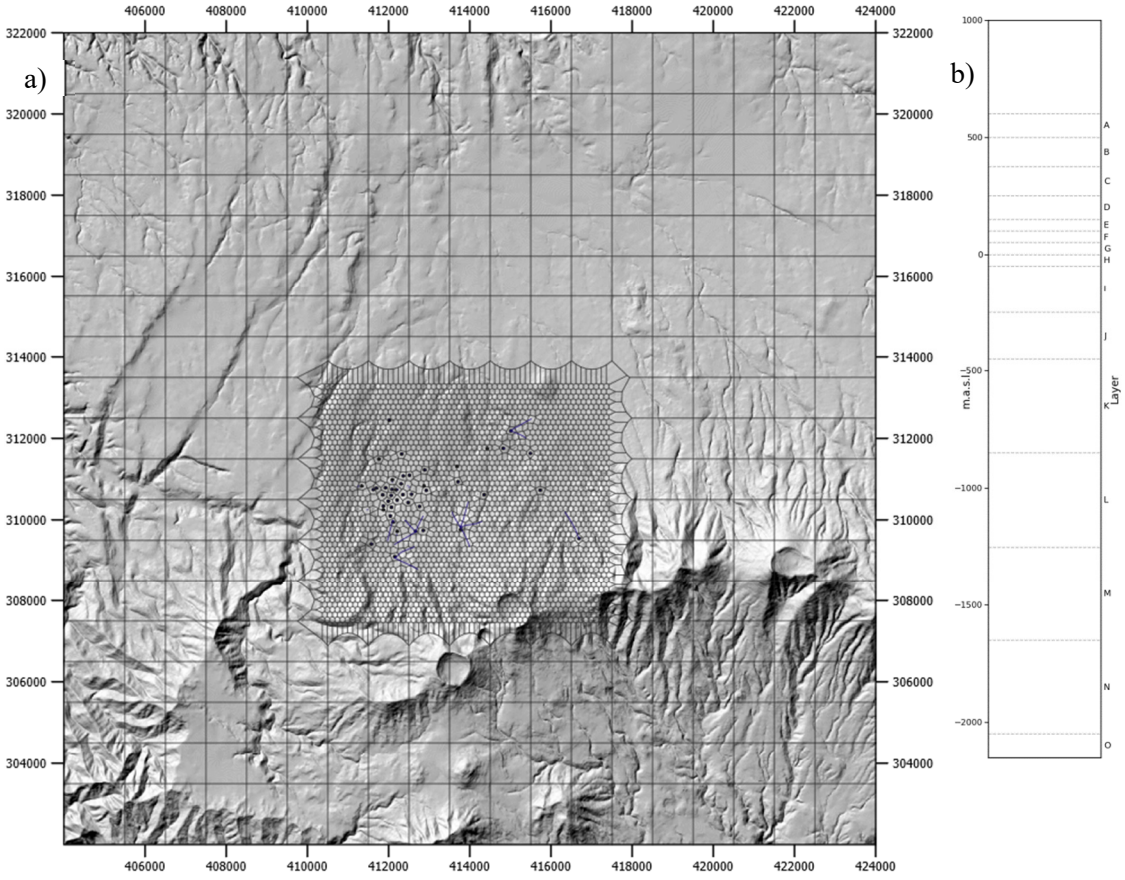

FIGURE 10: a) Mesh layout; and b) Layers distribution

A close view of the well field is shown in Figure 11.

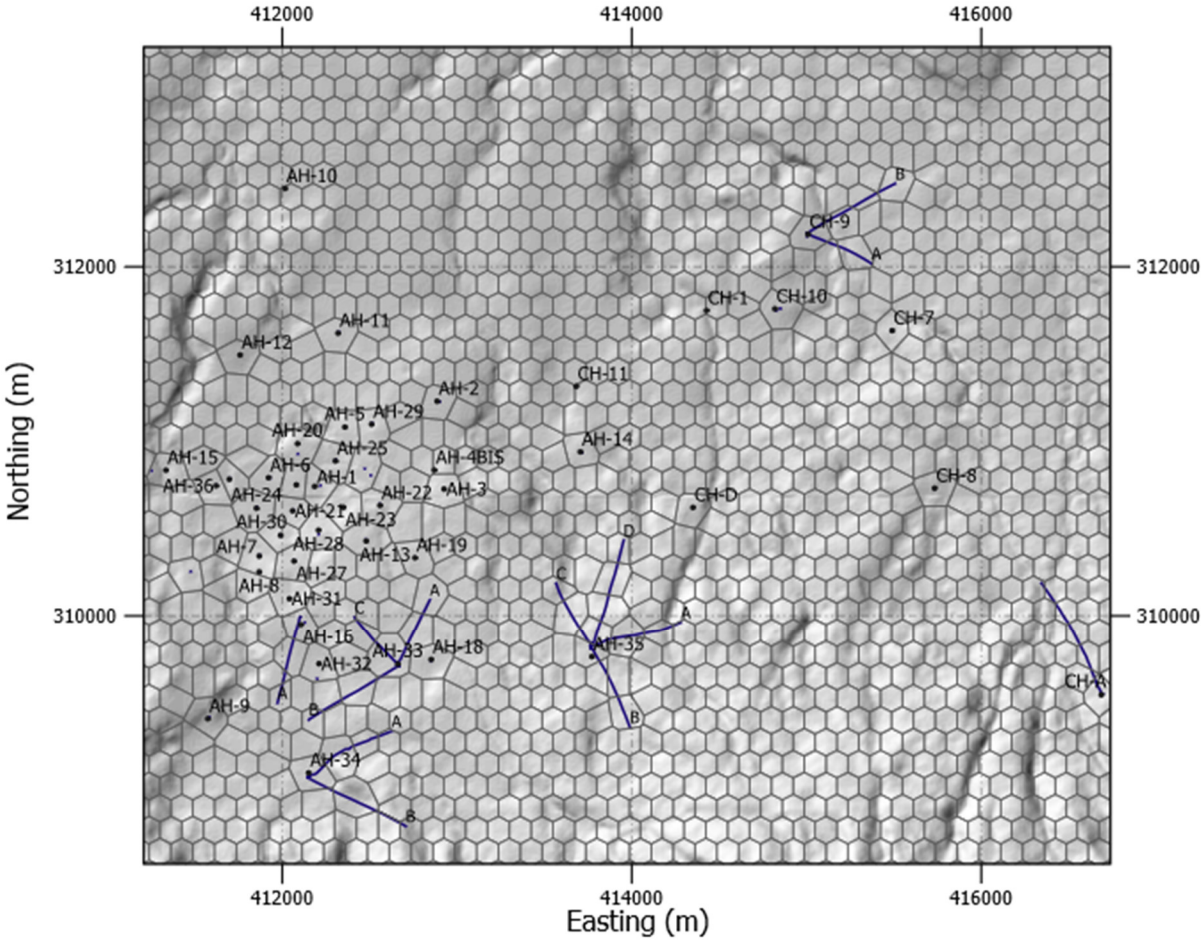

FIGURE 11: Well field

3.3.2 Vertical structure

The lithology and the formation temperature profiles are used to decide the number of layers, the thickness of each one and the elevation of the first layer.

The features of the layers are as follows. Layer A (surface) is located at 500 m a.s.l. and its thickness is 100 m. The cap rock, which relates to the young agglomerates, is in layer B which has a thickness of 125 m. Layers C to I have different rock type distributions based on the lithology. In the north part of the well field a steam cap is located and therefore, for some wells a different rock type is needed. The main features of this distribution are the andesites distributed all over layer C and the old agglomerates reaching from north to south replacing the andesites. The liquid zone, which is associated with old agglomerates, is in layers J to N, which have thicknesses of 200, 400, 400, 400 and 400 m, respectively. The deepest layer (layer M) is 100 m thick. The main feed zones of most of the wells are in the layers between the andesites and old agglomerates.

3.3.3 Rock properties

For all rock types the density is set at 2650 kg/m^3, the specific heat is 1000 J/kg°C, heat conductivity is 2.1 W/m°C and porosity 10 % (except for the OUTER rock type where the porosity is set to 8%). The permeability distribution for all rocks is listed in Table 2. These values are obtained by a trial and error procedure, as shown in Figure 9.

TABLE 2: Permeability values for each type of rock

Rock	PerX (mD)	PerY (mD)	PerZ (mD)	Description
BARRS	0.01	0.001	0.05	Barriers
BASEM	0.01	0.01	0.1	Bottom layer
OUTER	0.15	0.15	$1x10^{-3}$	Far-field
FAULT	150	150	150	Fault system
CHBAR	$1x10^{-5}$	$1x10^{-5}$	0.01	Chipilapa barrier
STEAM	100	100	400	High flowing enthalpy
STRES	90	90	80	Rocks within two-phase conditions
CHIRK	15	15	18	Chipilapa rocks
OLDAG	95	140	130	Old agglomerates
ANDEI	120	160	160	Andesites
YNGAG	0.01	0.01	0.01	Young agglomerate
SURFA	1	1	1	Surface

The permeability values and the rock type distribution are key elements in reproducing the initial conditions and consequently the production history of the geothermal field. Thus, the values shown in Table 2 are the result of an iteration process in order to match the natural state and the production history. Maps with the rock type distribution for all the layers is shown in Appendix I. The horizontal permeability for the rock type OUTER creates the conditions to imitate pressure support in the far-field.

3.3.4 Initial conditions

The model was initialized by using a thermal gradient of 70°C/km and a hydrostatic pressure profile corresponding to saturation conditions. The conditions at the surface are set to 34°C and 10 bar. The initial conditions are shown in Table 3.

TABLE 3: Initial conditions related with the far-field

Layer	Temperature (°C)	Pressure (bar)	Thickness (m)	Observation
A	34.5	10	100	Inactive
B	50.3	22	125	Perimeter inactive
C	59	34	125	Perimeter inactive
D	66	43	100	Perimeter inactive
E	69.5	48	50	Perimeter inactive
F	73	53	50	Perimeter inactive
G	76.5	57	50	Perimeter inactive
H	80	62	50	Perimeter inactive
I	94	80	200	Perimeter inactive
J	108	98	200	Perimeter inactive
K	136	132	400	Perimeter inactive
L	164	164	400	Perimeter inactive
M	192	193	400	Perimeter inactive
N	220	218	400	Perimeter inactive
O	227	224	100	Inactive

3.3.5 Boundary conditions

For all the elements in the top and bottom layers as well as the perimeter elements (far-field) from layer B to N, the pressure and temperature remain constant throughout the modelling (Dirichlet boundary conditions). Below the wellfield in the bottom layer, different temperatures are established on basis of the formation temperature. This setup is shown in Table 3.

3.3.6 Sink and sources

The heat source in the southern part of the field is spread over 19 grid blocks, each of them with a flow of 14 kg/s and an enthalpy of 1100 kJ/kg. The specified enthalpy corresponds to liquid saturation conditions at 255°C.

During the history matching, several sinks and sources were added to simulate the feed zones of the wells. These are located based on the actual the depths and horizontal coordinates of the wells' main feed zones. For the reinjection wells, both enthalpy and mass flow time-series are specified, while for the production wells, only the mass flow time-series are required (the enthalpy is computed by the simulator). To reduce the amount of input data, the time-series are resampled by calculating the weekly averages of the injection and production data. Of the sinks used to simulate the wells, 6 are on DELV (deliverability at constant bottomhole pressure), and 28 are on MASS (forced mass production). A total of 6 sources for DELV and 28 sources for MASS (forced mass production) are used.

The sinks and sources create the appropriate conditions around the wells to model the real conditions in the reservoir during the production history of the geothermal field.

3.3.7 Model parameters

The physical properties of the fluid are required to solve the equations describing the mass and energy balance. In TOUGH2, the physical properties are computed in modules called EOS (equation of state). For this work, the EOS1 is used which corresponds to pure water in liquid, vapor and two-phases conditions. EOS1 uses the steam table equation given by the International Formulation Committee in 1967 (Pruess et al., 1999). For the relative permeability Corey curves are selected. The immobile liquid saturation is set at 0.4 and the immobile gas saturation is set at 0.03 (Figure 12). For the capillary pressure function, a linear function is used.

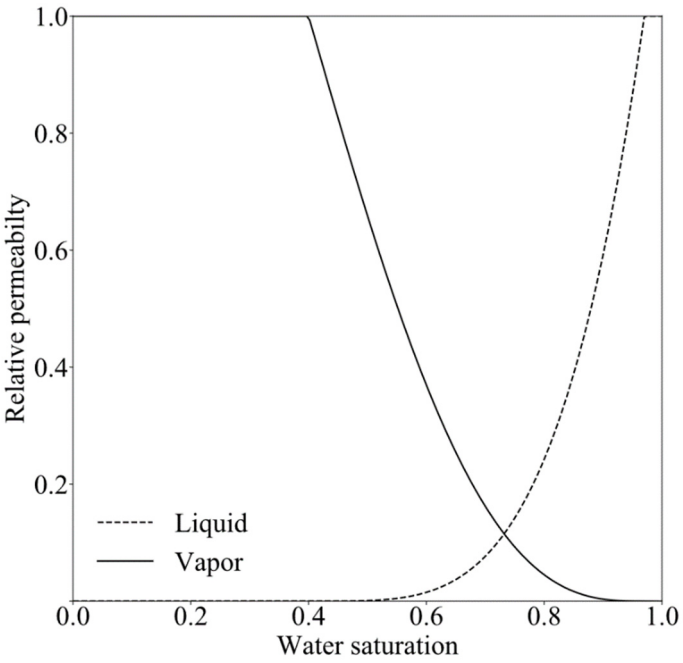

FIGURE 12: Relative permeability function

4. RESULTS

4.1 Parameter estimation

In the OBSERVATION block of iTOUGH2, the deviations are set to 5°C for temperature, 200 kJ/kg for enthalpy, and 5 bar for pressure and drawdown. The optimization was performed with 15 adjustable parameters: 7 horizontal and 6 vertical permeabilities, mass source inflow and flowing enthalpy of the source. For the permeabilities, it is the logarithm of the permeability that is adjusted as this usually leads to a more stable optimization. However, for the source-flow and -enthalpy, the values are adjusted directly. The flow is increased from the initial guess of 266 to 275.5 kg/s, the enthalpy was slightly increased from 1100 to 1111 kJ/kg. Figure 13 shows the comparison between the initial and modelled rock permeability.

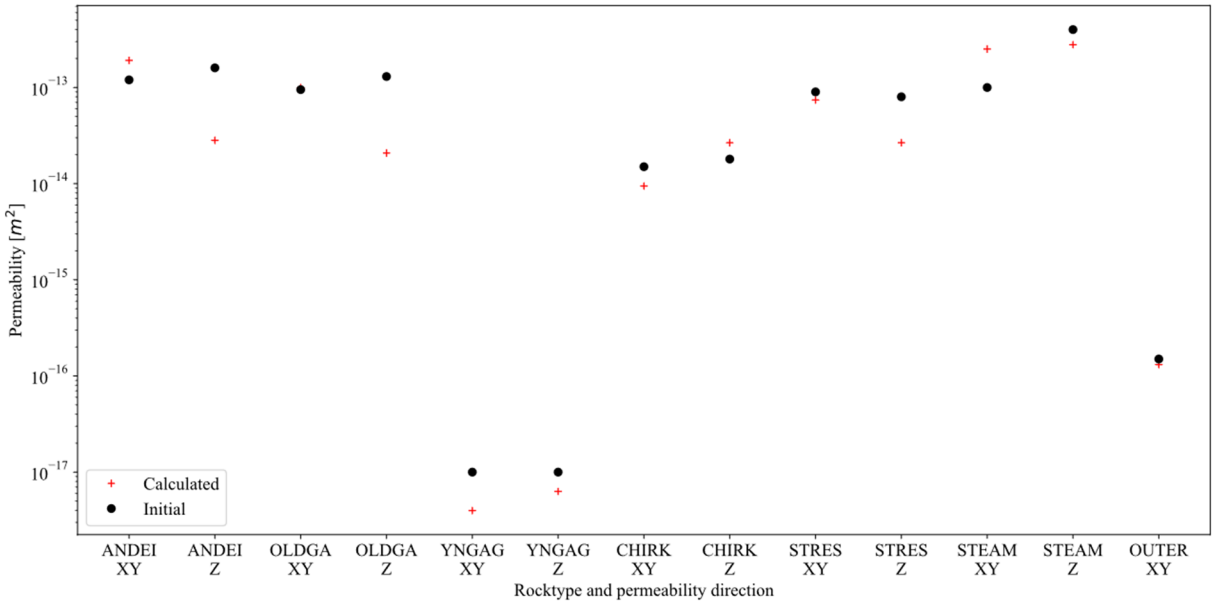

FIGURE 13: Initial and modelled rock permeability

4.2 Natural state fitting

During the natural state fitting the heat sources and fumaroles along with the rock distribution produce the necessary initial conditions (formation temperature, and pressure). In this trial and error calibration process, the key parameter to assess whether the natural state has been reached is the time step. When the time step reaches 10,000 years, it is assumed that the model has converged to a steady-state. This is selected by using the command STEADY-STATE in the iTOUGH2 input file. The results of the natural state simulations are shown in Appendix II.

Figure 14a shows the correlation between the measured and simulated temperature. The slope of the curve is 0.69 and the Pearson correlation coefficient is 0.67. During the modelling, the temperature of the top layer is fixed. These fixed values are not shown in Figure 15a. For the pressure, the correlation

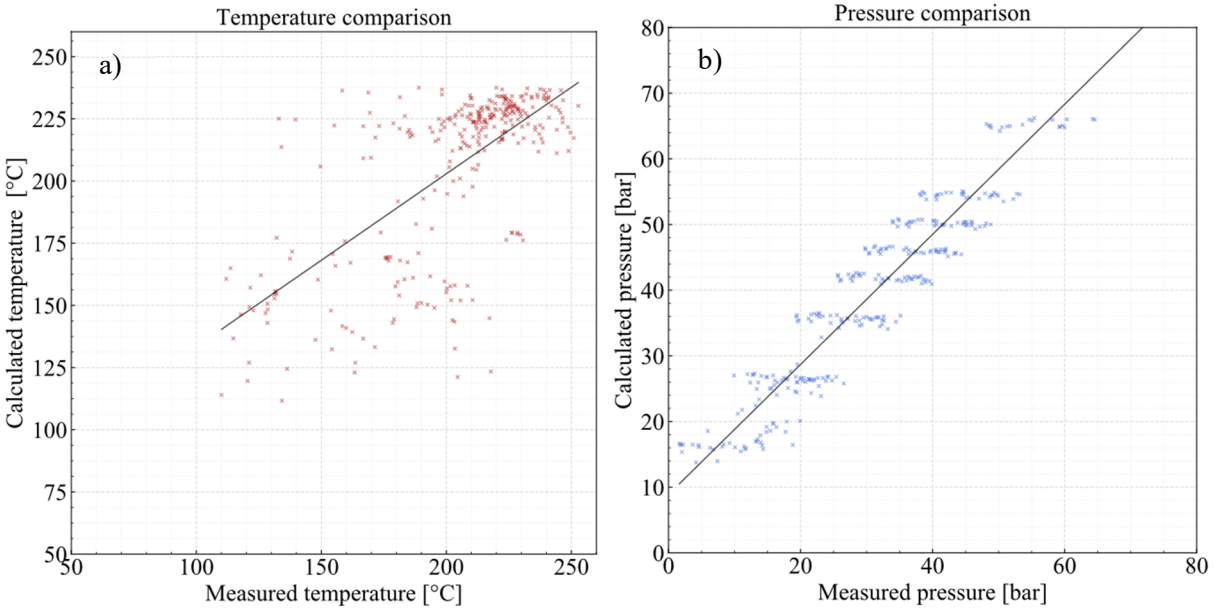

FIGURE 14: Comparison between observed and modelled
a) Downhole temperature; and b) pressure

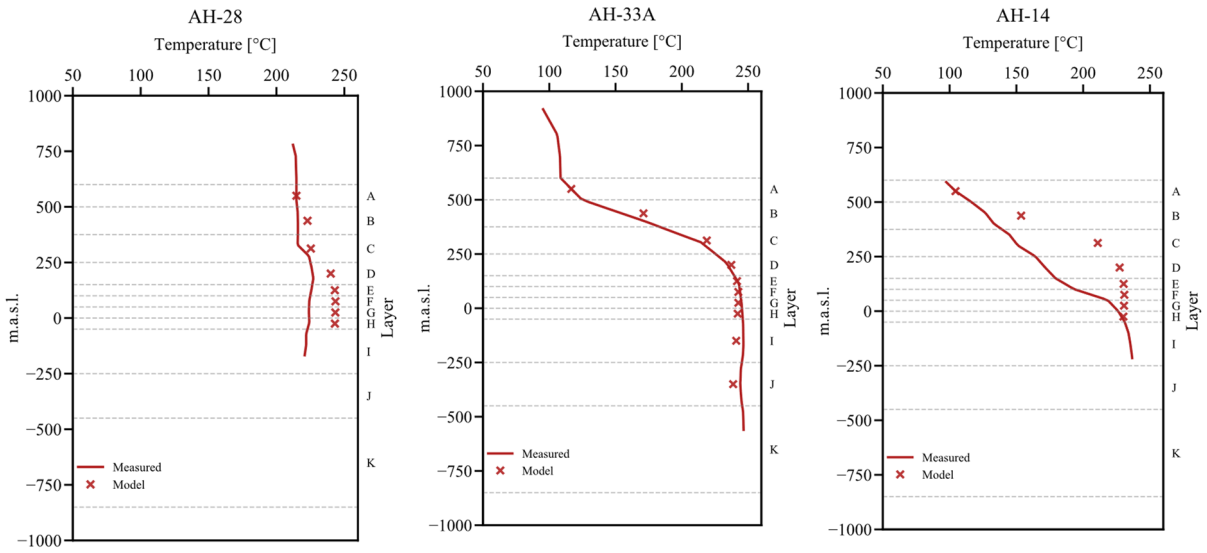

FIGURE 15: Measured and calculated temperature profiles in wells during natural state

is shown in Figure 14b. For these sets of data, the slope of the curve is 0.99 and the correlation coefficient is 0.97. From the figures in the Appendix II, it can be seen that generally a good match is obtained. For the wells concentrated in the northern area, the required isothermal conditions (boiling condition) are reached in wells AH-13 and AH-28 (Figure 15a). Furthermore, for some of the wells, such as wells AH-33A and AH-32 which have convective temperature profiles (Figure 15b), the temperature profiles are well reproduced in the model. However, for some other wells, the estimated temperature is too high, e.g. for AH-11. Another case where the initial conditions are not completely satisfied, are temperature profiles where thermal conduction dominates, as observed in wells AH-14, AH-34, AH-34A and AH-34B from layers B to D (Figure 15c).

4.3 Production history fitting

The natural state serves as a starting point for the production history model. Transient simulations are then performed to further improve the permeability distribution, boundary and initial conditions of the model, as shown in Figure 9. The monitoring well AH-25 is used as the main point of comparison to check for the pressure drawdown in the geothermal system. For the wells AH-1, AH-16A, AH-19, AH-20, AH-21, AH-22, AH-27, AH-28 and AH-31, the value of pressure is extracted from logs measured when the wells were shut-in or under bleeding conditions. Then, the pressure measured at 200 m a.s.l. is used to create time-series. Figure 16 shows an example of that. For pressure drawdown of the

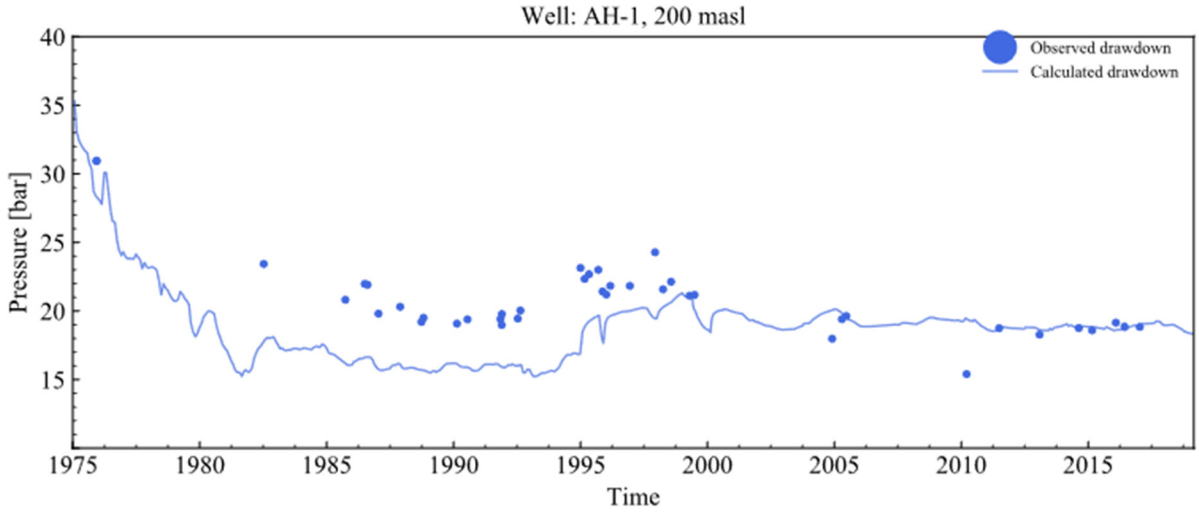

FIGURE 16: Comparison between observed and calculated pressure drawdown in well AH-1

remaining wells see Appendix III.

The flowing enthalpy of all the production wells is used for comparison during the production history matching. In this category, 26 wells are compared by extracting the enthalpy data from their corresponding feedzone elements. Figure 17 shows an example of the comparison between measured and calculated enthalpy. For all the wells with enthalpies lower than 1100 kJ/kg, good matches are obtained. For wells such as AH-6 or AH-17 where the flowing enthalpy corresponds to higher quality of steam, the calculated flowing enthalpy follows the trend but does not reach the high values that have been measured. All the flowing enthalpy comparison figures can be found in Appendix III.

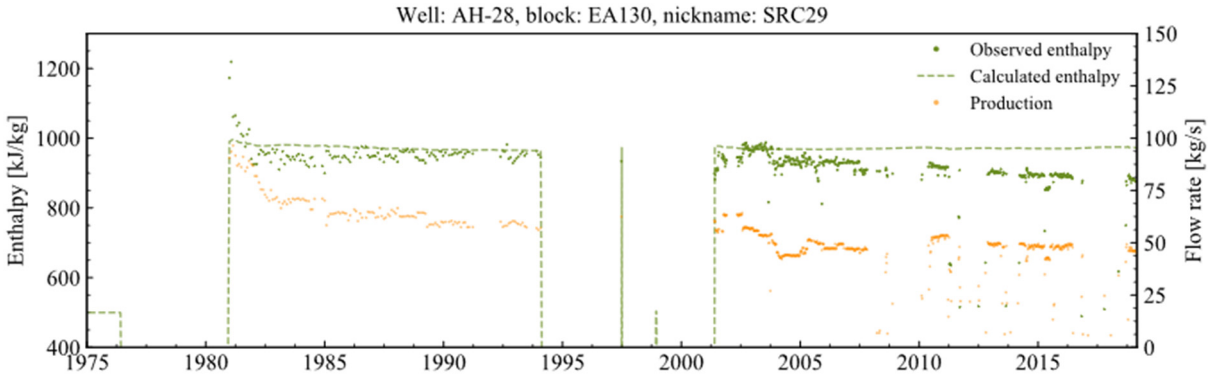

FIGURE 17: Comparison between observed and calculated enthalpy for well AH-28

4.4 Forecast

A 20 years forecast was modelled, maintaining the current exploitation status of the production and reinjection wells. It can be seen in Figure 18 that the pressure decline is very slow during this period, this behaviour is characteristic of an open system (Axelsson, 2012). The pressure decline is about 1.5 bar over the 20-year period.

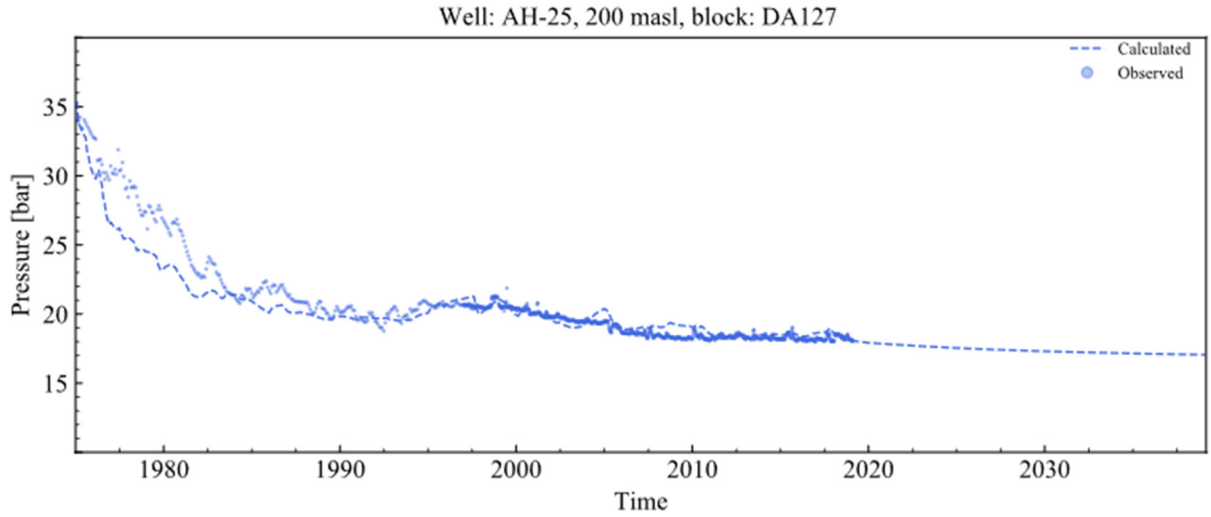

FIGURE 18: Forecast for pressure drawdown in monitoring well AH-25

Figure 19 shows the behaviour of the enthalpy during the forecast period, the value is stable. However, the model does not reproduce flowing enthalpies higher than 1100 kJ/kg. Similar graphs for additional wells are shown in Appendix IV.

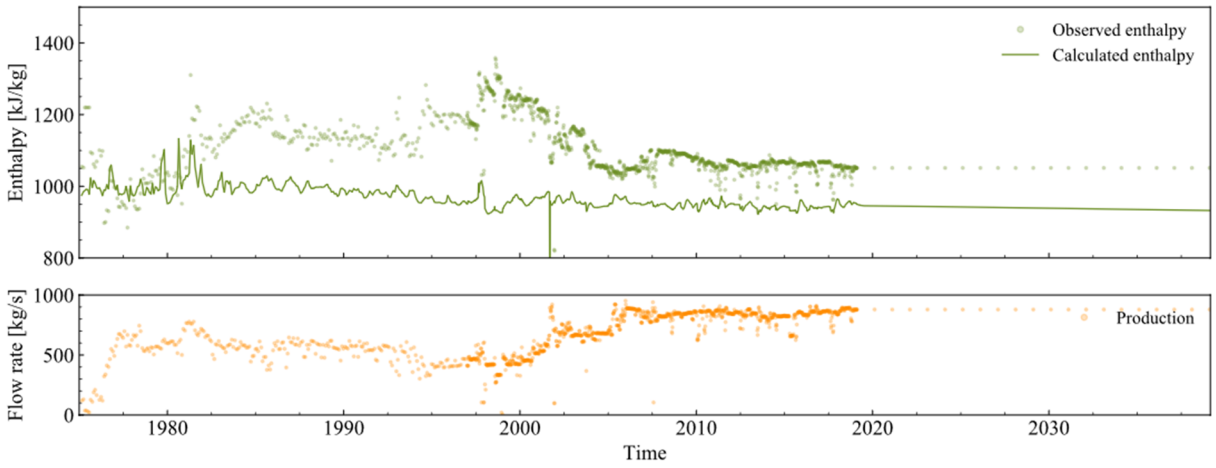

FIGURE 19: Weighted enthalpy forecast and total production

5. DISCUSSION

Due to the exploitation of the geothermal resource, the thermodynamic conditions in the reservoir change over time. Thus, the monitoring of wells plays a very important role in understanding the nature and response of the geothermal system to utilization (Axelsson, 2016). The pressure, temperature and steam quality forecast are an indication of how the geothermal system will behave in the future.

Cooling due to exploitation is revealed in all the wells. Figure 20 shows the behaviour of well AH-20, the temperature decrease is estimated to be 3°C during the 20-year period.

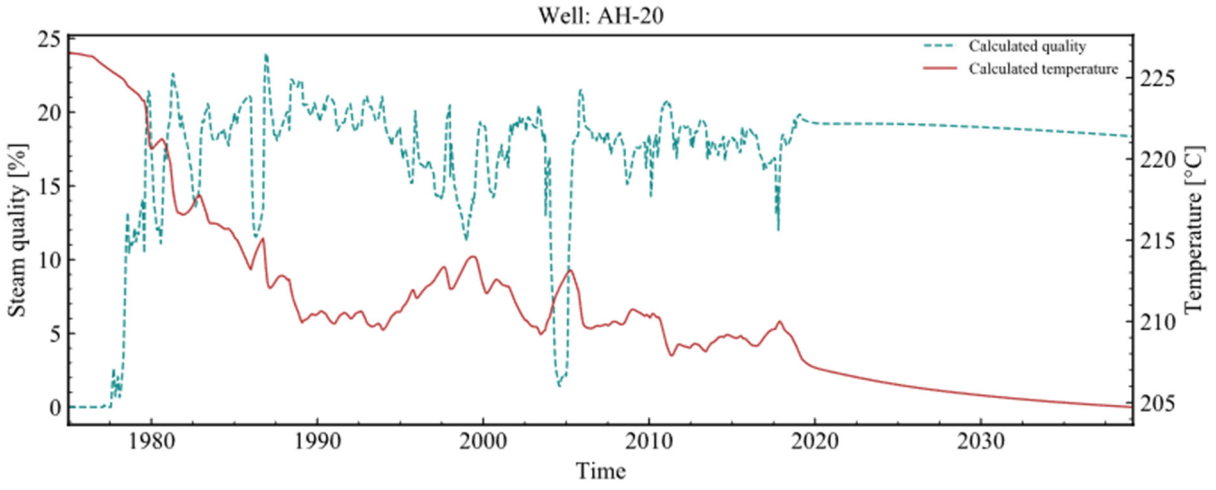

FIGURE 20: Calculated temperature and steam quality conditions at the AH-20 feed zone

In the model, the southern wells show sharp change in temperature, which could indicate non-stabilized conditions, and the temperature there is still decreasing at end of the forecast (Figure 21). Despite the fact that the pressure and temperature are still decreasing at that time, the difference between the initial and final values for the period are 0.5 bar and 2°C respectively, which are small values for a time period of 20 years.

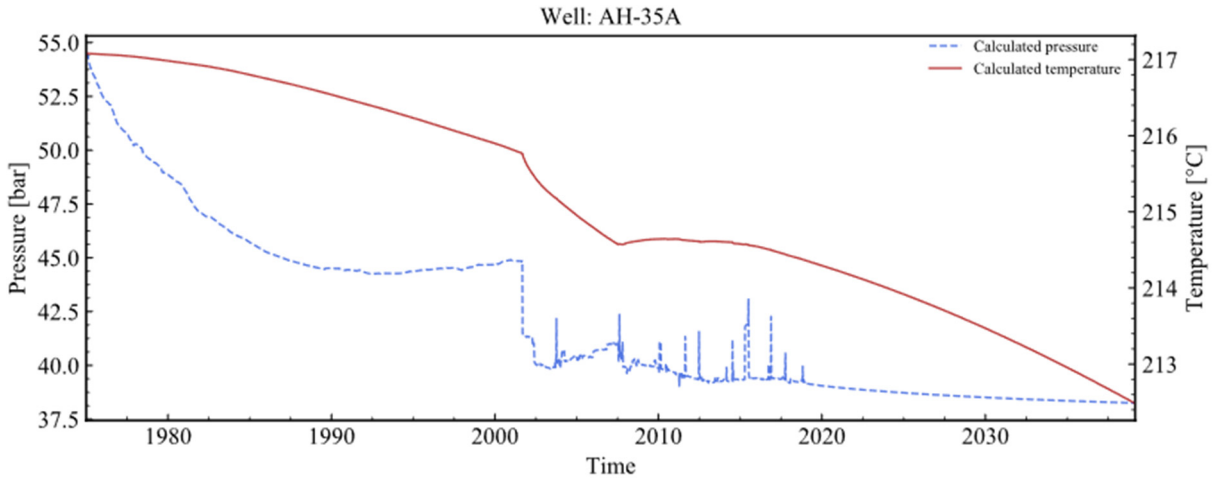

FIGURE 21: Calculated pressure and temperature at AH-35A feed zone

Considering the main findings of the model, stable conditions of production for the next 20 years are forecasted. However, it is important to mention that scaling effects are not included in the modelling. Thus, make-up wells might be needed in the future.

6. CONCLUSIONS AND RECOMMENDATIONS

This study has described the development of a detailed numerical model for the Ahuachapán geothermal field in El Salvador, using the TOUGH2 simulator. It consists of 45,300 elements in 15 layers and 28,684 datapoints. The rock type distribution in the model is based on the latest conceptual model of the geothermal system and known lithologic distribution. The model is used to forecast the reservoir performance over the next 20 years. The main conclusions of this work are:

- According to the lithologic data and formation temperature integrated in Leapfrog Geothermal, the Ahuachapán andesites (main reservoir rock) are found at greater depth in the southern part of the geothermal field which is correlated to high temperatures.
- The heat sources, permeability distribution and barriers included in the numerical model, based on the current conceptual model, were able reproduce the natural state conditions and the pressure decline observed in response to the production and reinjection in the field.
- The permeabilities around the wells range from 15 to 160 mD for the horizontal permeabilities and from 13 to 80 mD for the vertical values.
- Under the current exploitation conditions, the model predicts a 1.5 bar pressure decline in monitoring well AH-25 over the next 20 years. Therefore, maintaining the current production rate is feasible.
- Based on the pressure trend due to exploitation, the Ahuachapán geothermal field can be categorized as an open system.
- The inverse modelling performed for the current setting confirmed the values used for the rock permeabilities and heat source flow rate and enthalpy.

Finally, the modelling tools used and developed in this study should be used and further improved to assist with the sustainable management of the current and future geothermal fields in El Salvador.

ACKNOWLEDGEMENTS

I would like to express my gratitude to the UNU-GTP staff, Mr. Lúdvík S. Georgsson, Mr. Ingimar G. Haraldsson, Ms. Málfrídur Ómarsdóttir, Mr. Markús A. G. Wilde, Ms. Thórhildur Ísberg and Dr. Vigdís Hardardóttir for their care, advice and assistance. Sincere thanks to my supervisors Andri Arnaldsson, Jean-Claude Berthet and Lárus Thorvaldsson from Vatnaskil Consulting Engineers for their guidance and sharing of experience throughout my project.

Thanks to my employer LaGeo for granting me leave to undertake this training, specially to the staff at the reservoir engineering department to share their knowledge. Thank you all 2019 UNU fellows, in particular to Shi Meng, John, Mubashir and Vivi for the company, fun and support during this period.

Finally, I want to express my gratitude to my family for the moral support during these months.

REFERENCES

Aunzo, Z., Bödvarsson, G.S., Laky, C., Lippmann, M.J., Steingrímsson, B., Truesdell, A.H., and Witherspoon, P.A., 1989: *The Ahuachapán geothermal field, El Salvador. Reservoir analysis*. Lawrence Berkeley Laboratory, Earth Sciences Division, Berkeley, CA, report LBL-26612, 199 pp.

Axelsson, G., 2012: The physics of geothermal energy. In: Sayigh, A. (ed.), *Comprehensive renewable energy*, Vol. 7, Elsevier, Oxford, 3–50.

Axelsson, G., 2016: Sustainable management of geothermal resources. *Presented at "SDG Short Course I on Sustainability and Environmental Management of Geothermal Resource Utilization and the Role of Geothermal in Combating Climate Change", organized by UNU-GTP and LaGeo, Santa Tecla, El Salvador*, 15 pp.

Bödvarsson, G.S., and Witherspoon, P.A., 1989: Geothermal reservoir engineering, part 1. *Geotherm. Scie & Tech, 2-1,* 1-68.

Cuéllar, G., Choussy, M., and Escobar, D.,1981: Extraction-reinjection at Ahuachapán geothermal field. In: Rybach, L., and Muffler, L.J.P., (editors), *Geothermal systems. Principles and case histories.* John Wiley and Sons Ltd., Chichester, 321-336.

ENEL-LaGeo, 2004: *Feasibility study for the optimization and developments of Ahuachapan, Chipilapa and Cuyanausul geothermal systems - report on Ahuachapan – Chipilapa conceptual model and drilling proposals*. ENEL and LaGeo, Santa Tecla, internal report, 264 pp.

Finsterle, S., 2007: *iTOUGH2 User's Guide.* Lawrence Berkeley National Laboratory, Lawrence Berkeley National Laboratory, Earth Sciences Division, Berkeley, CA, 291 pp.

Finsterle, S., 2015: *iTOUGH2 V7.0 Command Reference.* Lawrence Berkeley National Laboratory, Earth Sciences Division, Berkeley, CA, 130 pp.

Grant, M., and Bixley, M., 2011: *Geothermal reservoir engineering*. Elsevier, Cambridge, MA, 349 pp.

Haukwa, C., 1998: *AMESH: a mesh creating program for the integral finite difference method. User's manual*. Lawrence Berkeley National Laboratory, Lawrence Berkeley National Laboratory, Earth Sciences Division, Berkeley, CA, 54 pp.

LaGeo, 2010: *Numerical model update for Ahuachapán* (in Spanish). LaGeo, Santa Tecla, El Salvador, internal report.

LaGeo, 2019: *Geothermal management system database*. LaGeo, Santa Tecla, El Salvador, internal source.

Laky, C., Lippmann, M.J., Bödvarsson, G.S., Retana, M., and Cuellar, G., 1989: Hydrogeologic model of the Ahuachapán geothermal field, El Salvador. *Proceedings of the 14th Workshop on Geothermal Reservoir Engineering, Stanford University, Stanford, CA*, 265-272.

Leapfrog, 2019: *3D geological modelling software*. Leapfrog, webpage: *www.leapfrog3d.com/*

Montalvo L., F.E., 1996: Tracer modelling and heat mining calculations for the Ahuachapán geothermal field El Salvador C.A. Report 2 in: *Geothermal Training in Iceland 1996.* UNU-GTP, Iceland, 1-22.

Monterrosa, M. and Montalvo L., F.E., 2006: Geothermal reservoir management in El Salvador case histories of Ahuachapán and Berlín, *Presented at Workshop for Decision Makers on Geothermal Projects in Central America, organized by UNU-GTP and LaGeo*, *Santa Tecla, El Salvador,* 15 pp.

Monterrosa M., and Montalvo L., F.E., 2010: Sustainability analysis of the Ahuachapán geothermal field: management and modelling. *Geothermics*, *39*, 370-381.

O'Sullivan, M., Pruess, K. and Lippman, M., 2000: Geothermal reservoir simulation: The state-of-practice and emerging trends. *Proceedings of the World Geothermal Congress 2000, Kyushu-Tohoku, Japan*, 4065-4069.

Pedrazzi, D., Sunye-Puchol, I., Aguirre-Diaz, G, Costa, A., Smith, V., Poret, M., Harris, P., Miggins, D., Hernandez, W. and Gutierrez., E., 2019: The Ilopango Tierra Blanca Joven (TBJ) eruption, El Salvador: Volcano-stratigraphy and physical characterization of the major Holocene event of Central America. *J. Volcanology and Geothermal Research*, *377,* 81-102.

Pruess, K., 2002: *Mathematical modelling of fluid and heat transfer in geothermal systems – an introduction in five lectures.* UNU-GTP, Iceland, report 3, 92 pp.

Pruess, K., Oldenburg, C., and Moridis, G., 1999, revised 2012: *TOUGH2, User's Guide, Version 2.0.* Lawrence Berkeley National Laboratory, Earth Sciences Division, Berkeley, CA, 197 pp.

Python Software Foundation, 2019: *Python language reference, version 2.7*. Python Software, webpage: *docs.python.org/2/*

Santos, P., 2010: Contribution of Magneto-Telluric method to geothermal development in El Salvador, *Proceedings of the World Geothermal Congress 2010, Bali, Indonesia*, 6 pp.

Santos, P., and Rivas, A., 2009: Gravity surveys contribution to geothermal exploration in El Salvador: the cases of Berlín, Ahuachapán and San Vicente areas. *Presented at "Short Course on Surface Exploration for Geothermal Resources", organized by UNU-GTP and LaGeo, in Ahuachapán and Santa Tecla, El Salvador*, 6 pp.

Truesdell, A., Aunzo, Z., Bödvarsson, G., Alonso, J. and Campos, A., 1989: The use of Ahuachapan fluid chemistry to indicate natural state conditions and reservoir processes during exploitation. *Proceedings of the 14th Workshop on Geothermal Reservoir Engineering, Stanford University, Stanford, CA*, 273-278.

Unidad de Transacciones S.A. de C.V., 2019: *Statistical Bulletin* (in Spanish). Unidad de Transacciones S.A. de C.V., Santa Tecla, El Salvador, 39 pp.

Vatnaskil Consulting Engineers, 2015: *Steinar 7.7.* Vatnaskil Consulting Engineers, website: *www.vatnaskil.is/steinar*

APPENDIX I: Rock distribution in different layers

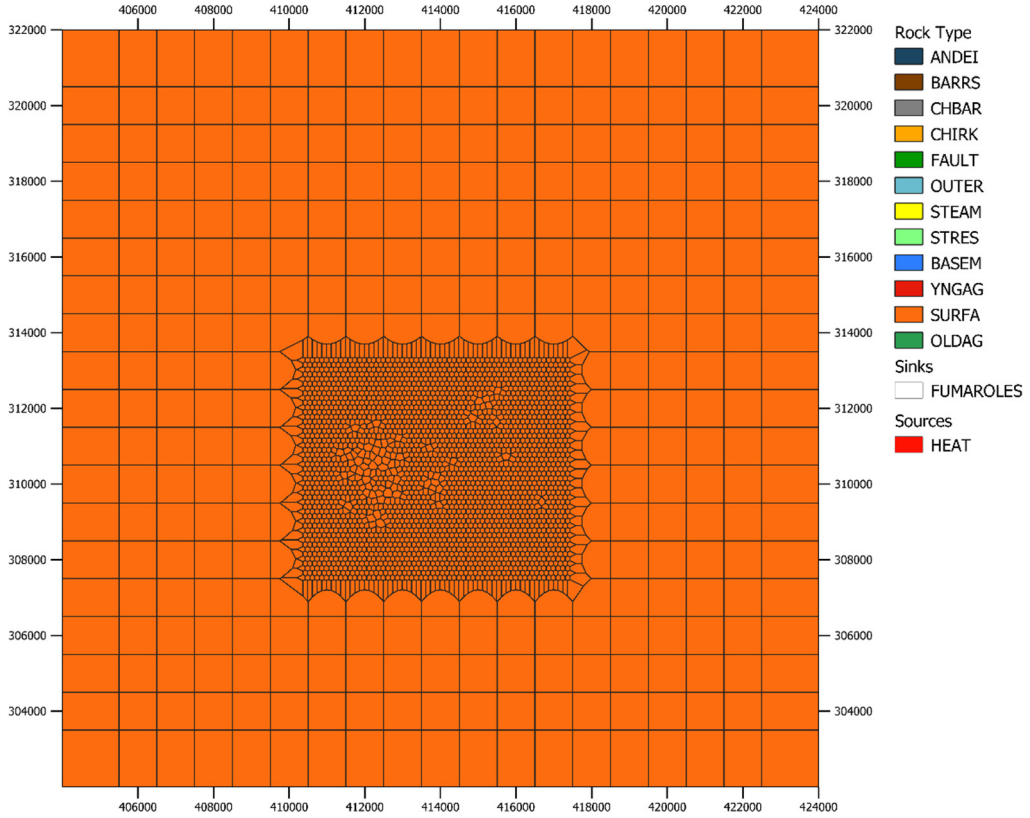

FIGURE 1: Layer 1 - rock distribution

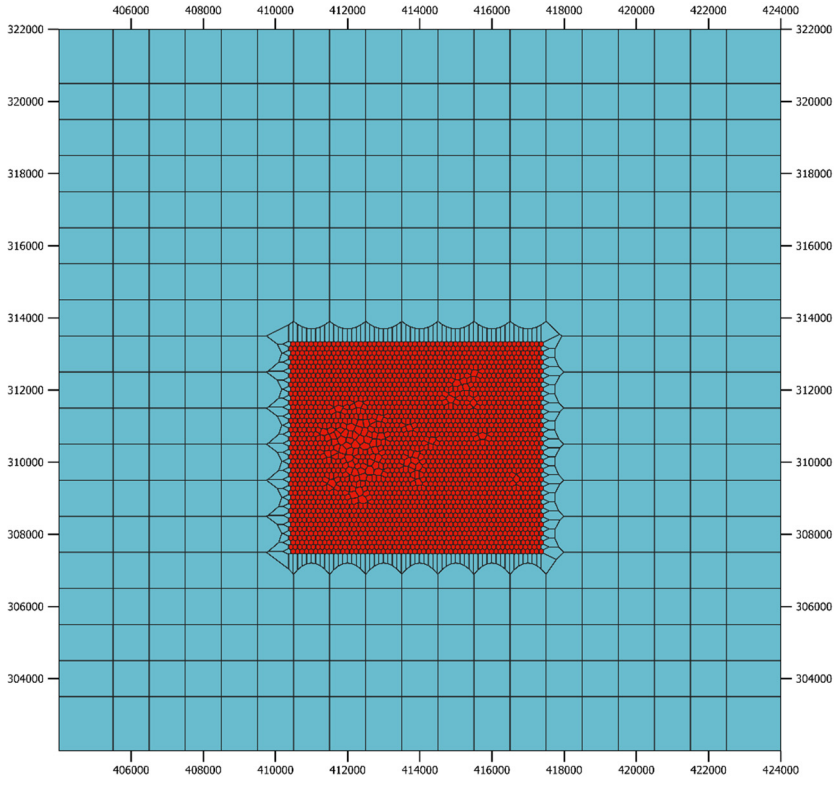

FIGURE 2: Layer 2 - rock distribution

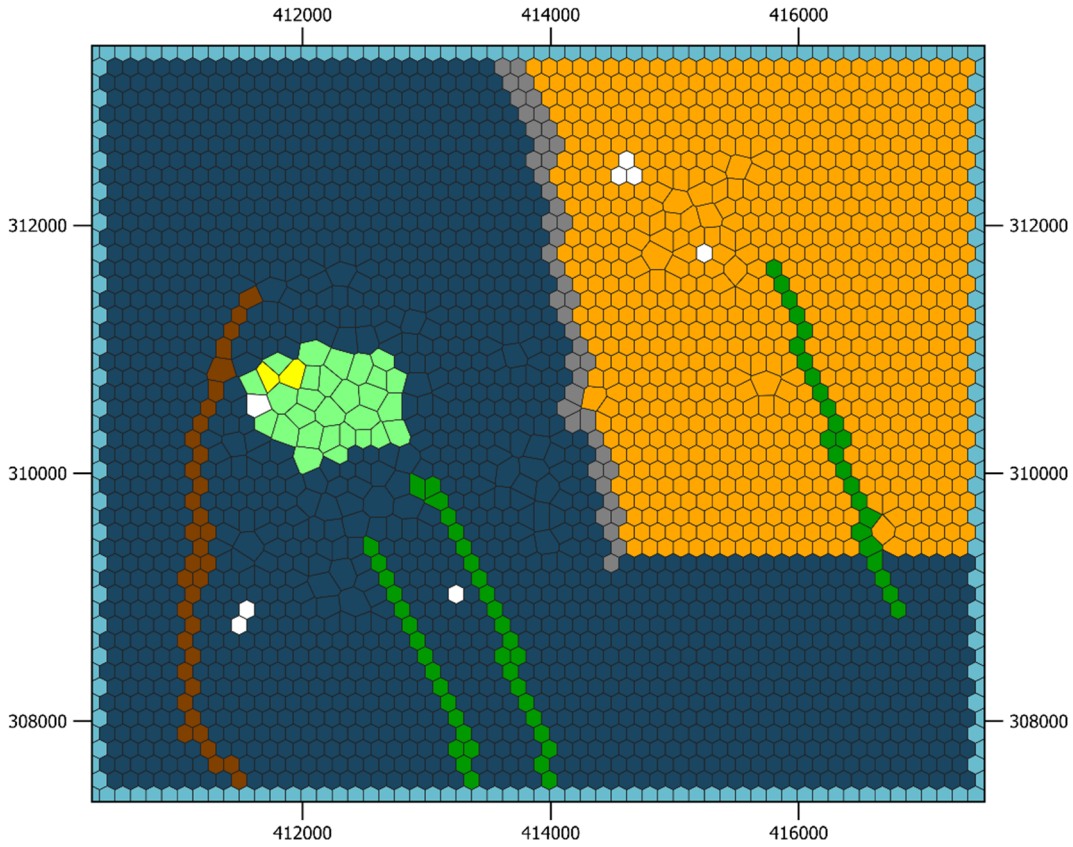

FIGURE 3: Layer 3 - the extension has been reduced to have a clear view of the wellfield

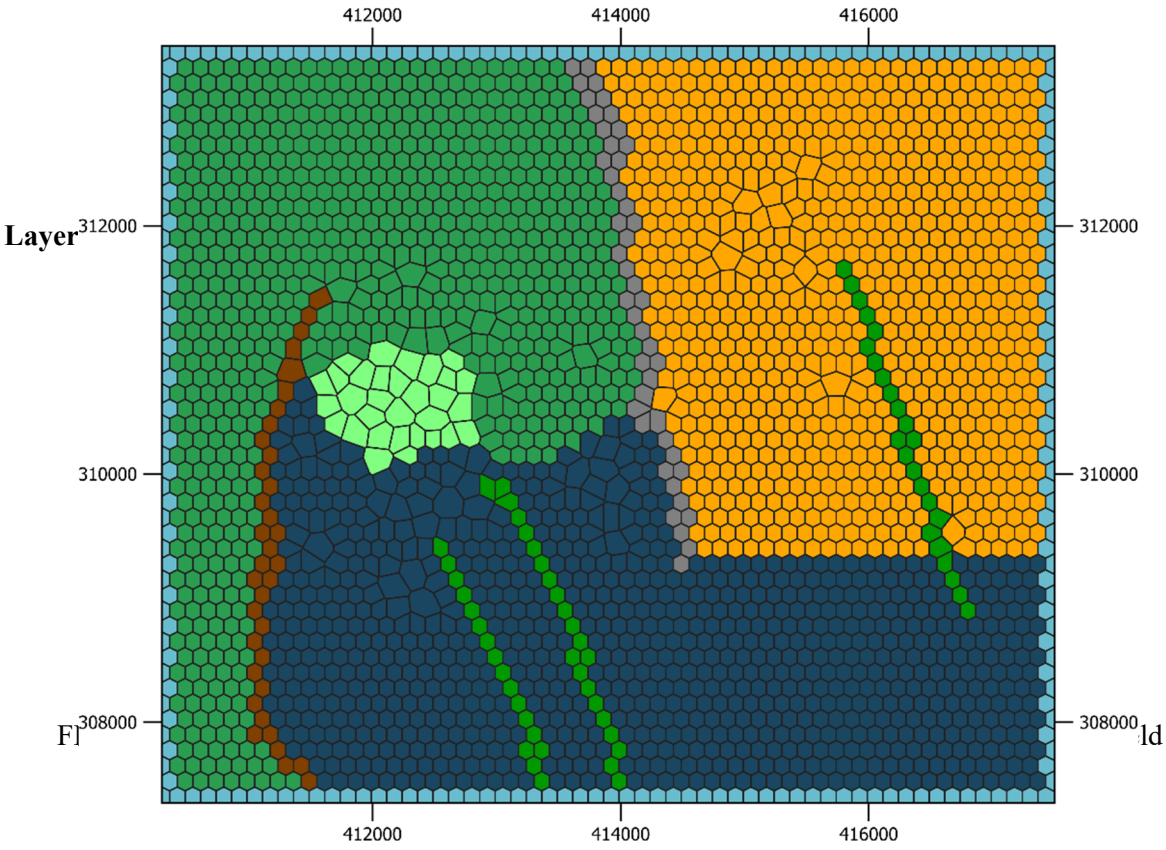

FIGURE 4: Layers 4-7 - the extension has been reduced to have a clear view of the wellfield

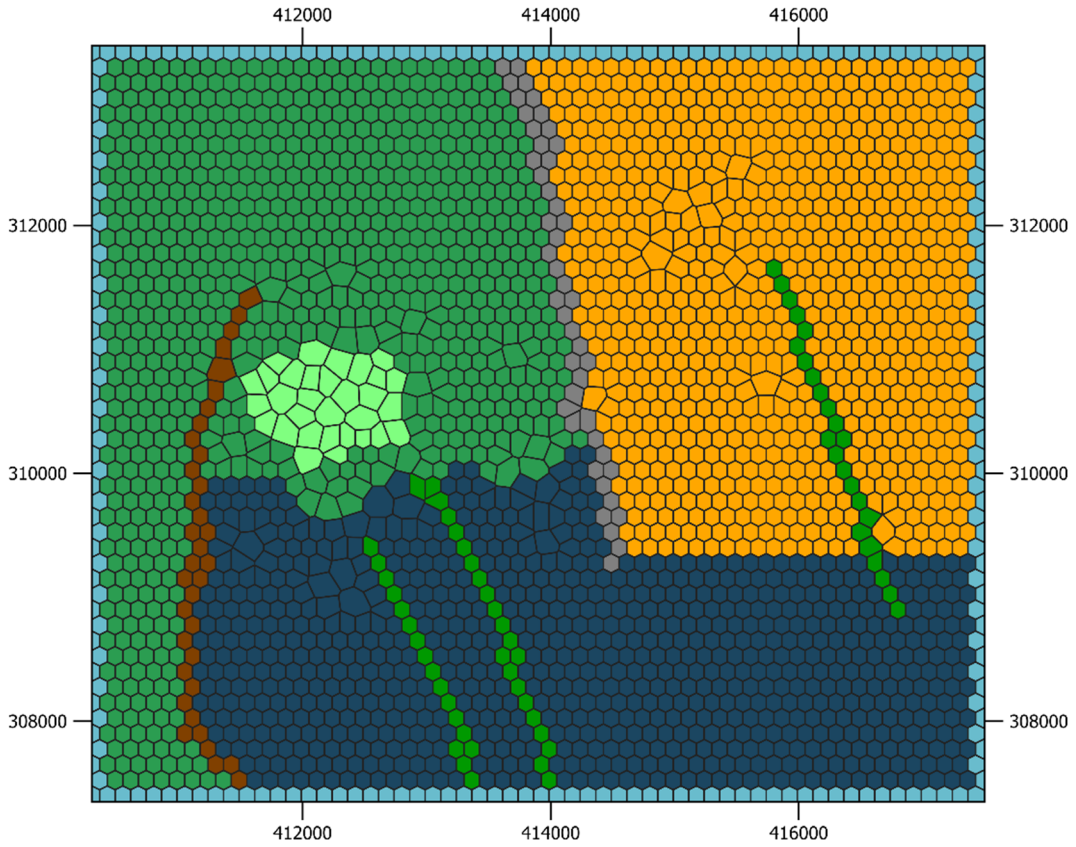

FIGURE 5: Layers 8 and 9 - the extension has been reduced to have a clear view of the wellfield

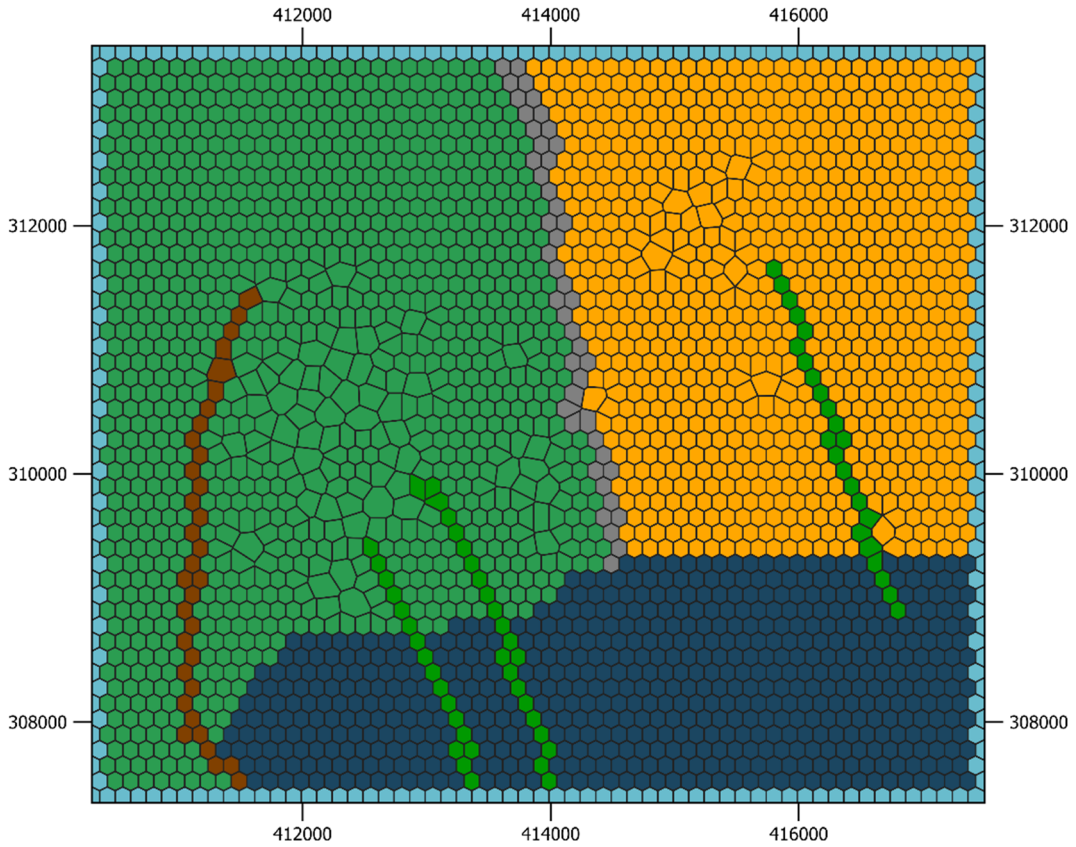

FIGURE 6: Layer 10 - the extension has been reduced to have a clear view of the wellfield

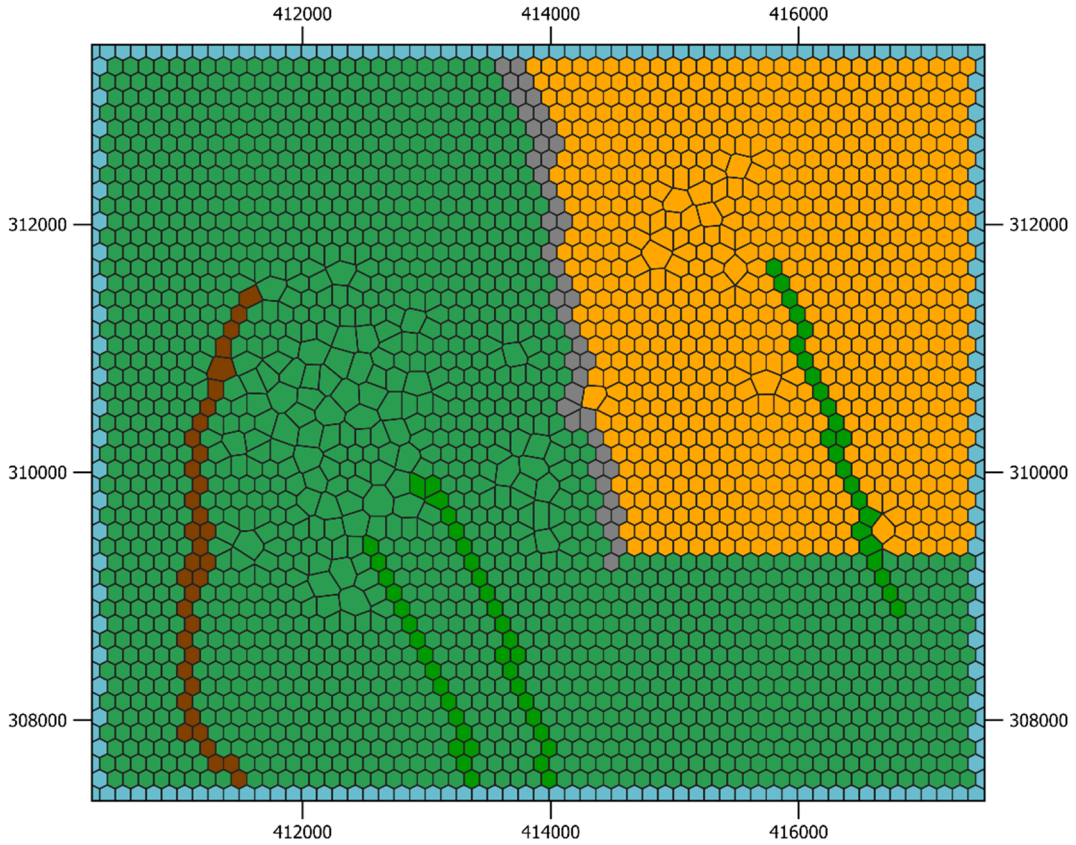

FIGURE 7: Layers 11-13 - the extension has been reduced to have a clear view of the wellfield

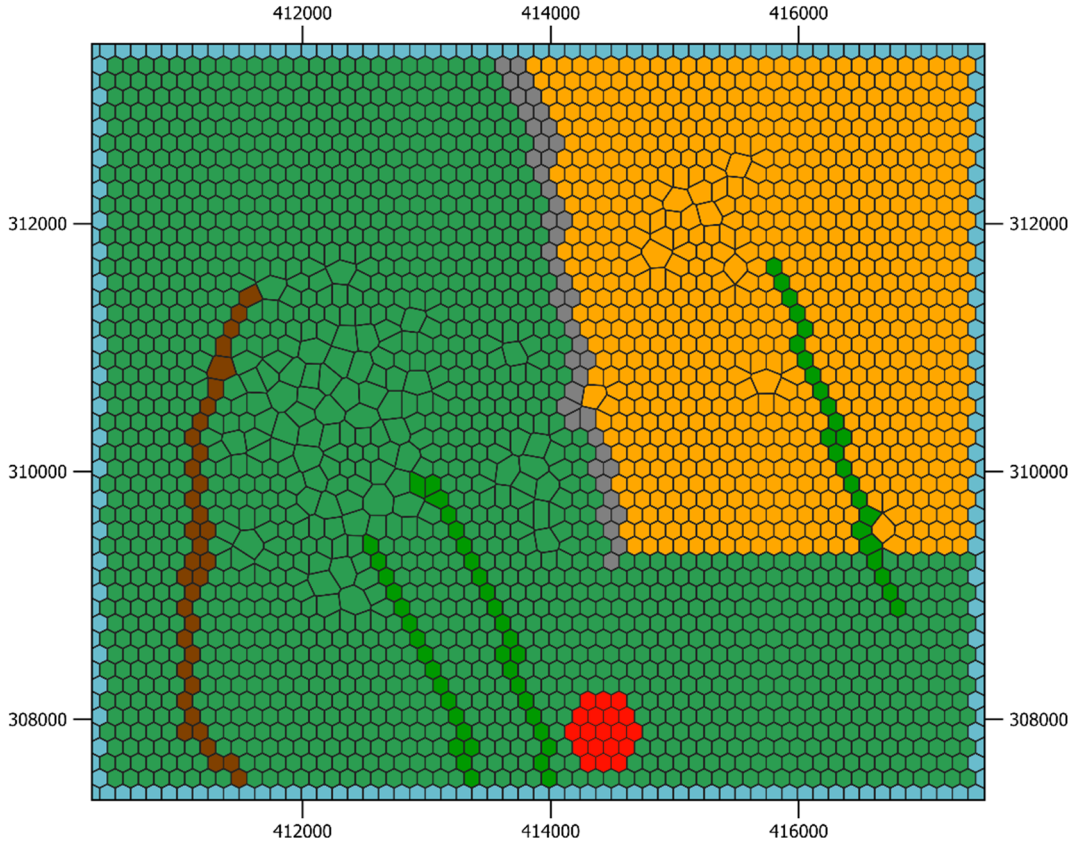

FIGURE 8: Layer 14 - the extension has been reduced to have a clear view of the wellfield

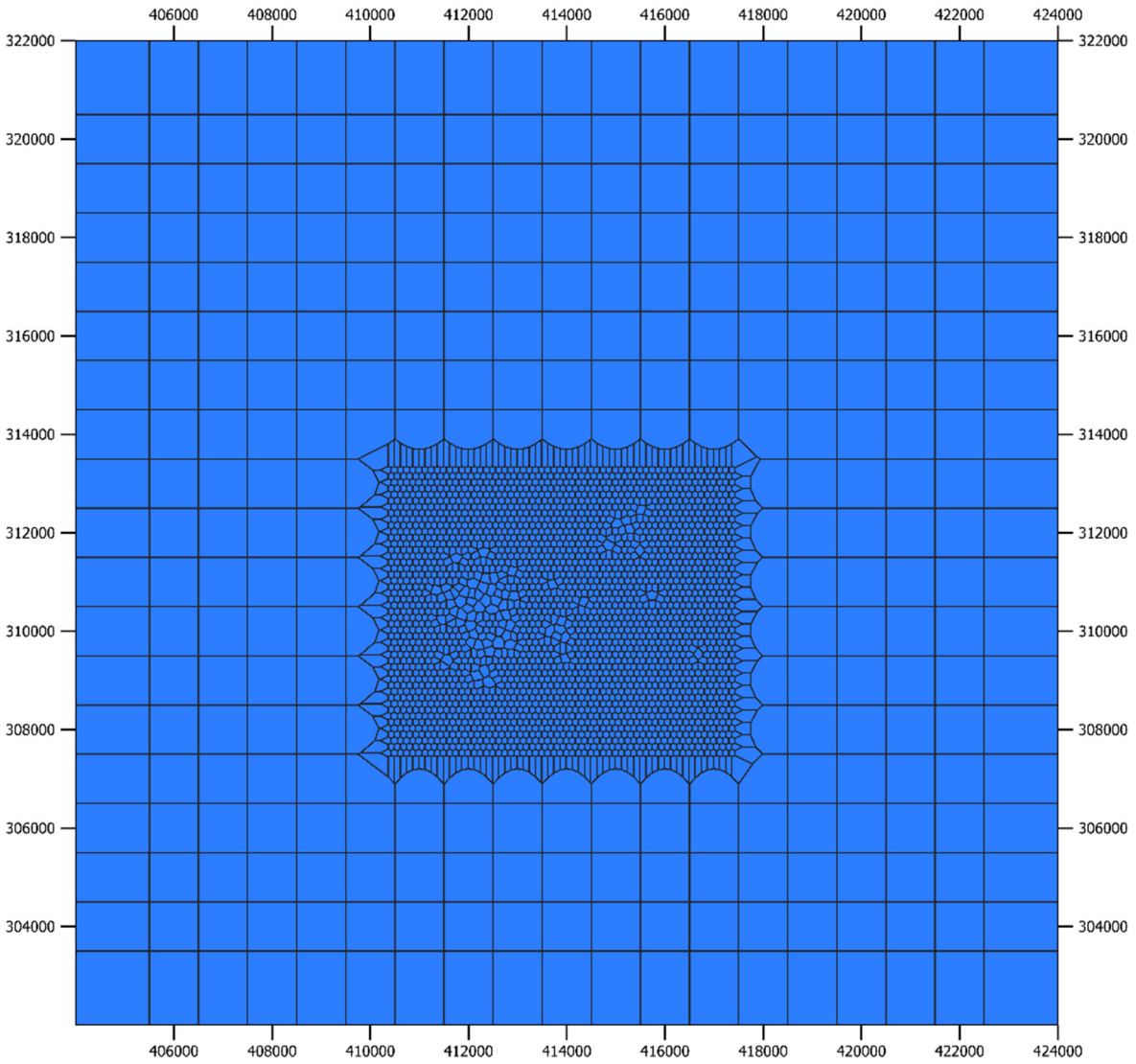

FIGURE 9: Layer 15 – rock distribution

APPENDIX II: Comparison of measured and calculated natural state temperature profiles for each well in the Ahuachapán geothermal field

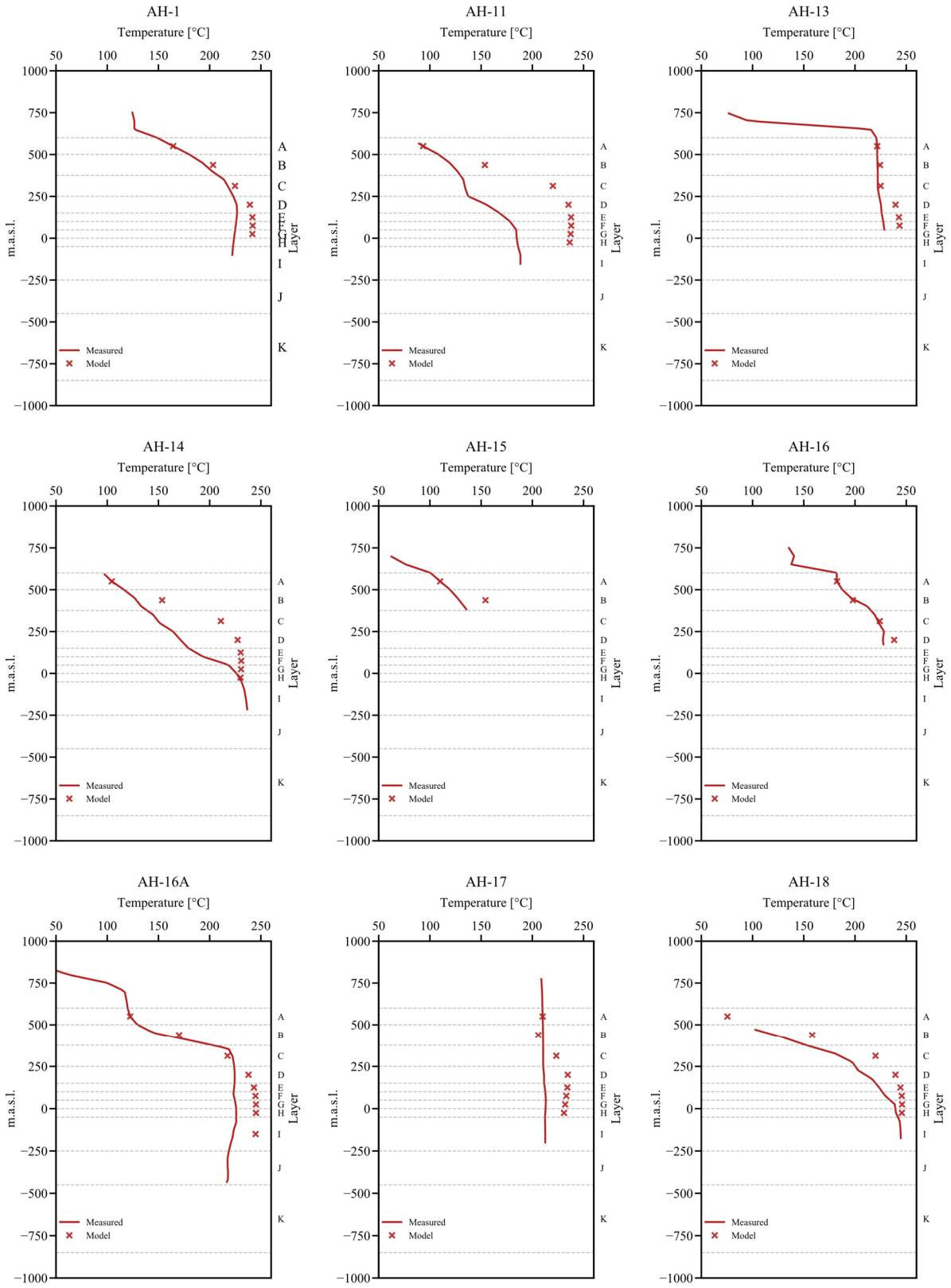

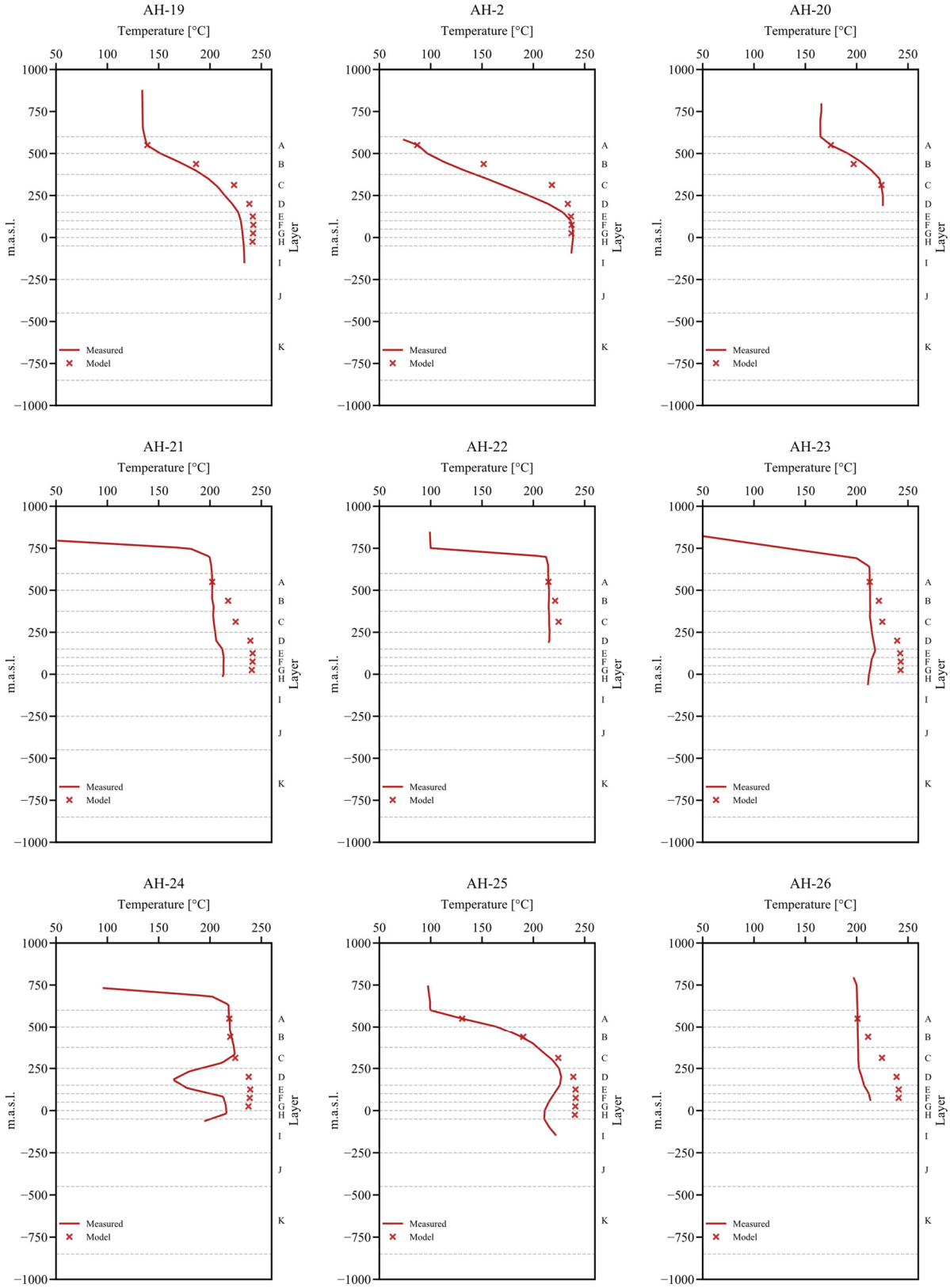
AH-19
AH-2
AH-20
AH-21
AH-22
AH-23
AH-24
AH-25
AH-26
Temperature [°C]
50
100
150
200
250
m.a.s.l.
1000
750
500
250
0
−250
−500
−750
−1000
Layer
A
B
C
D
E
F
G
H
I
J
K
Measured
Model

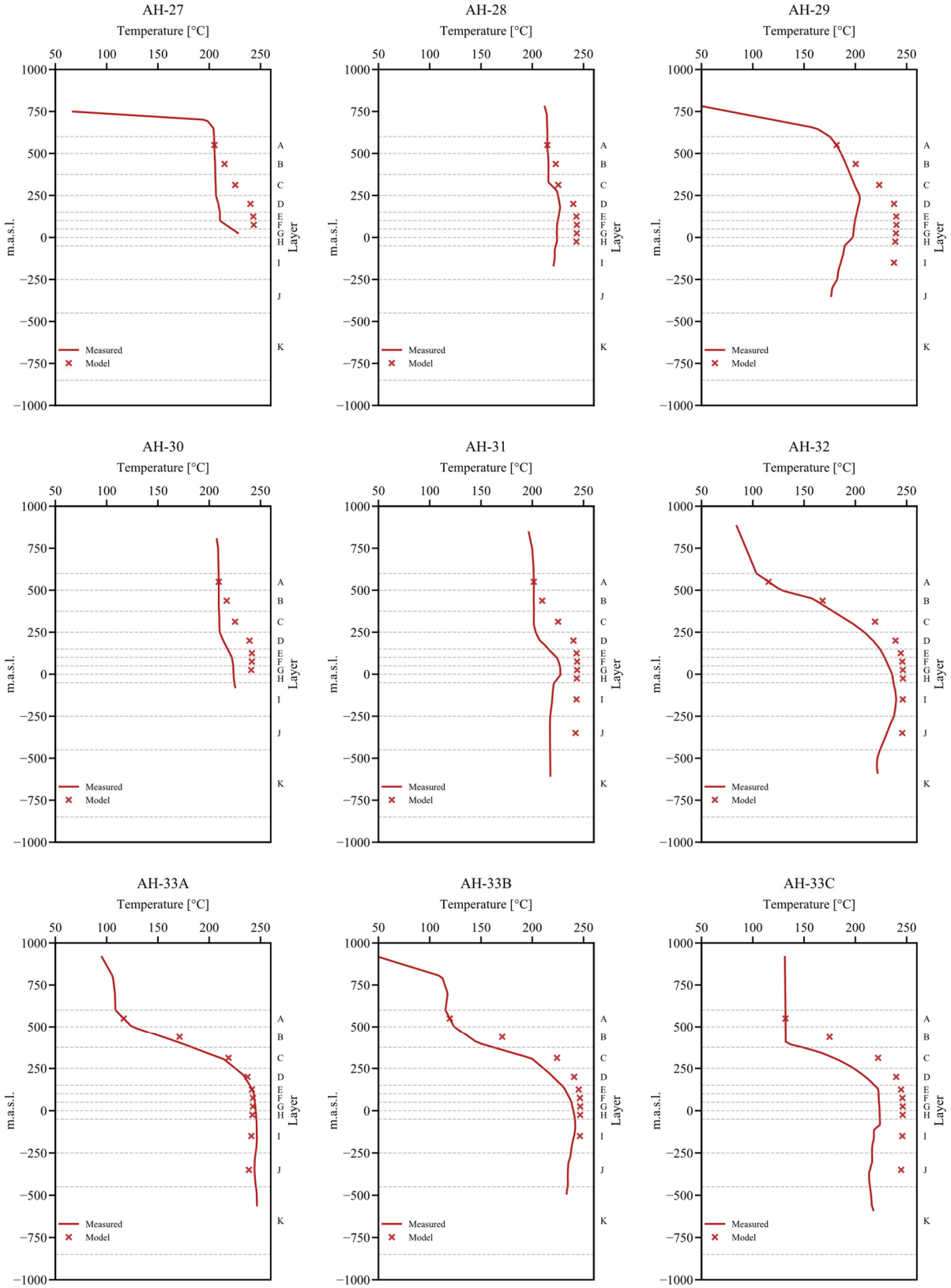
AH-27
AH-28
AH-29
AH-30
AH-31
AH-32
AH-33A
AH-33B
AH-33C
Temperature [°C]
50
100
150
200
250
m.a.s.l.
1000
750
500
250
0
−250
−500
−750
−1000
Layer
A
B
C
D
E
F
G
H
I
J
K
Measured
Model

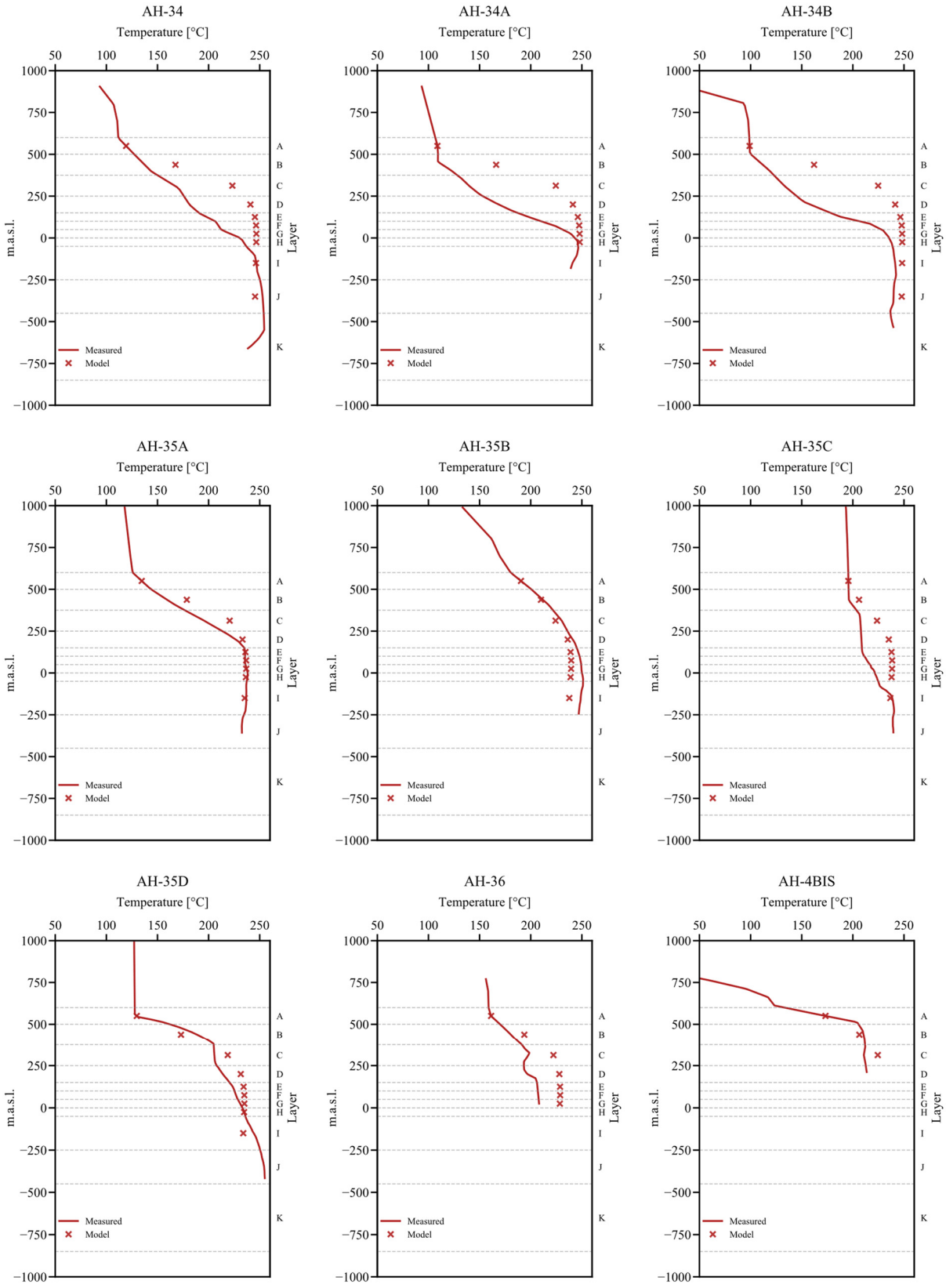
AH-34
AH-34A
AH-34B
AH-35A
AH-35B
AH-35C
AH-35D
AH-36
AH-4BIS
Temperature [°C]
50
100
150
200
250
1000
750
500
250
0
−250
−500
−750
−1000
m.a.s.l.
A
B
C
D
E
F
G
H
I
J
K
Layer
Measured
Model

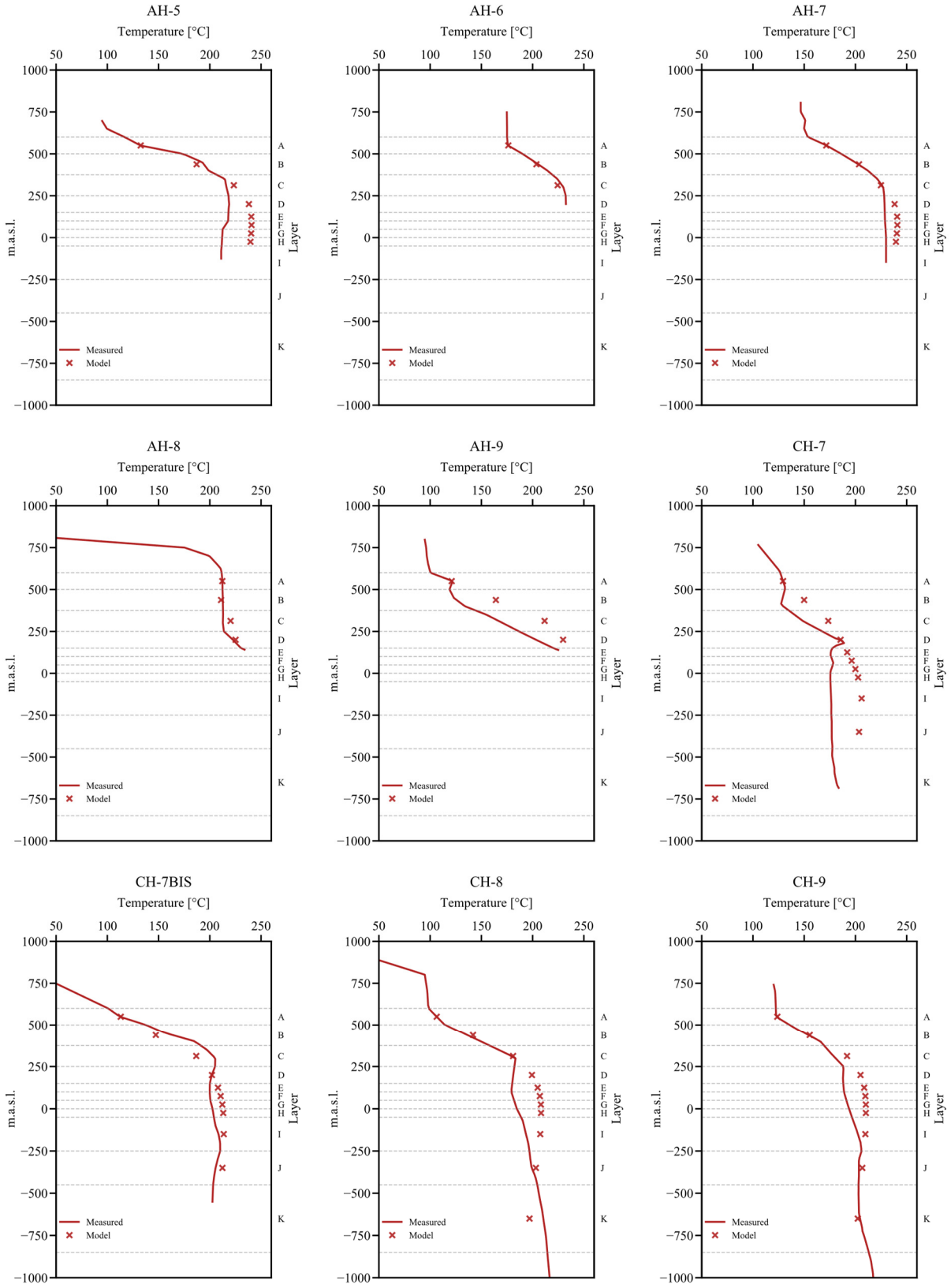
AH-5
AH-6
AH-7
AH-8
AH-9
CH-7
CH-7BIS
CH-8
CH-9
Temperature [°C]
50
100
150
200
250
1000
750
500
250
0
−250
−500
−750
−1000
m.a.s.l.
A
B
C
D
E
F
G
H
I
J
K
Layer
Measured
Model

APPENDIX III: Comparison between observed and calculated flowing enthalpy

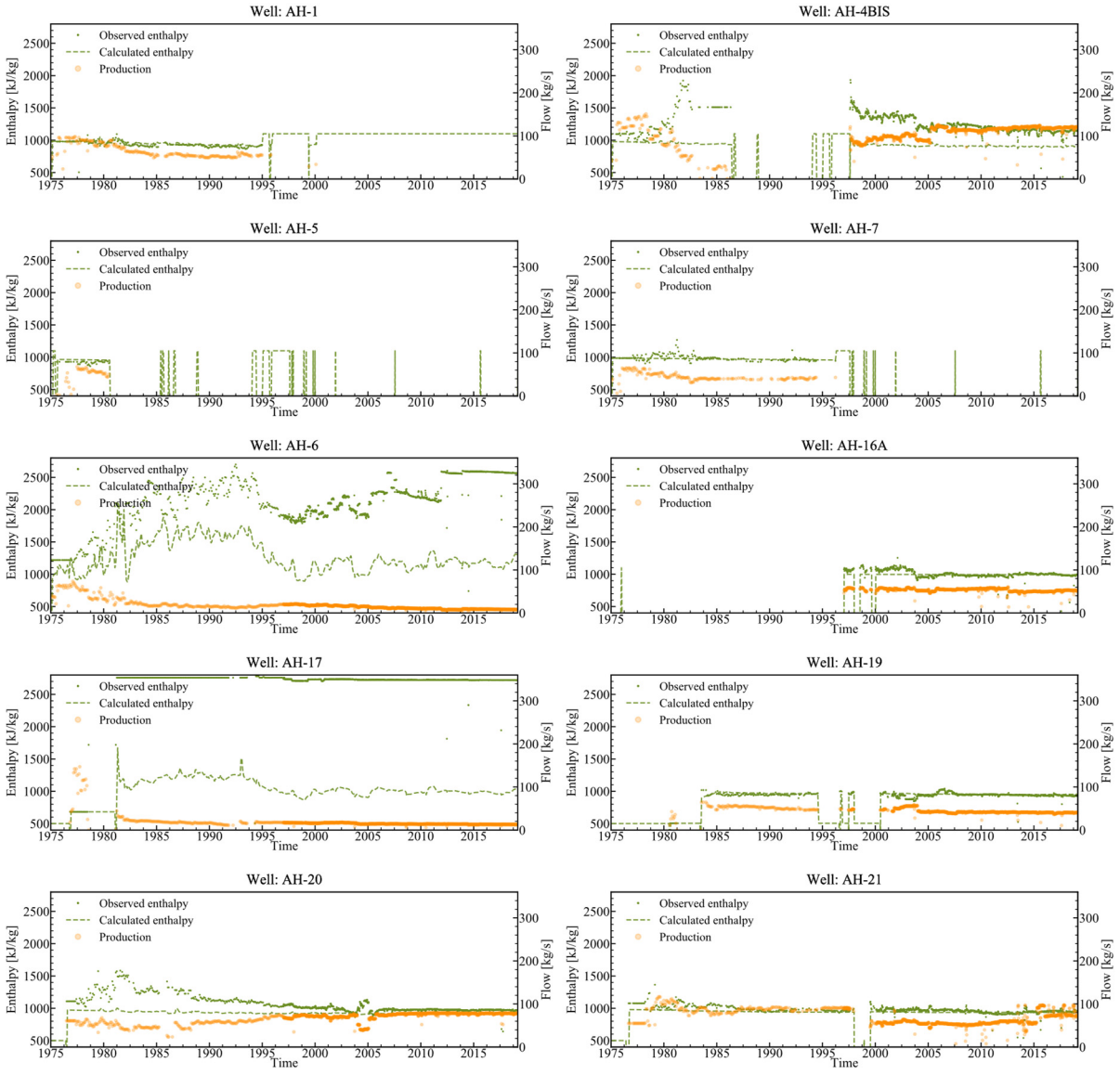

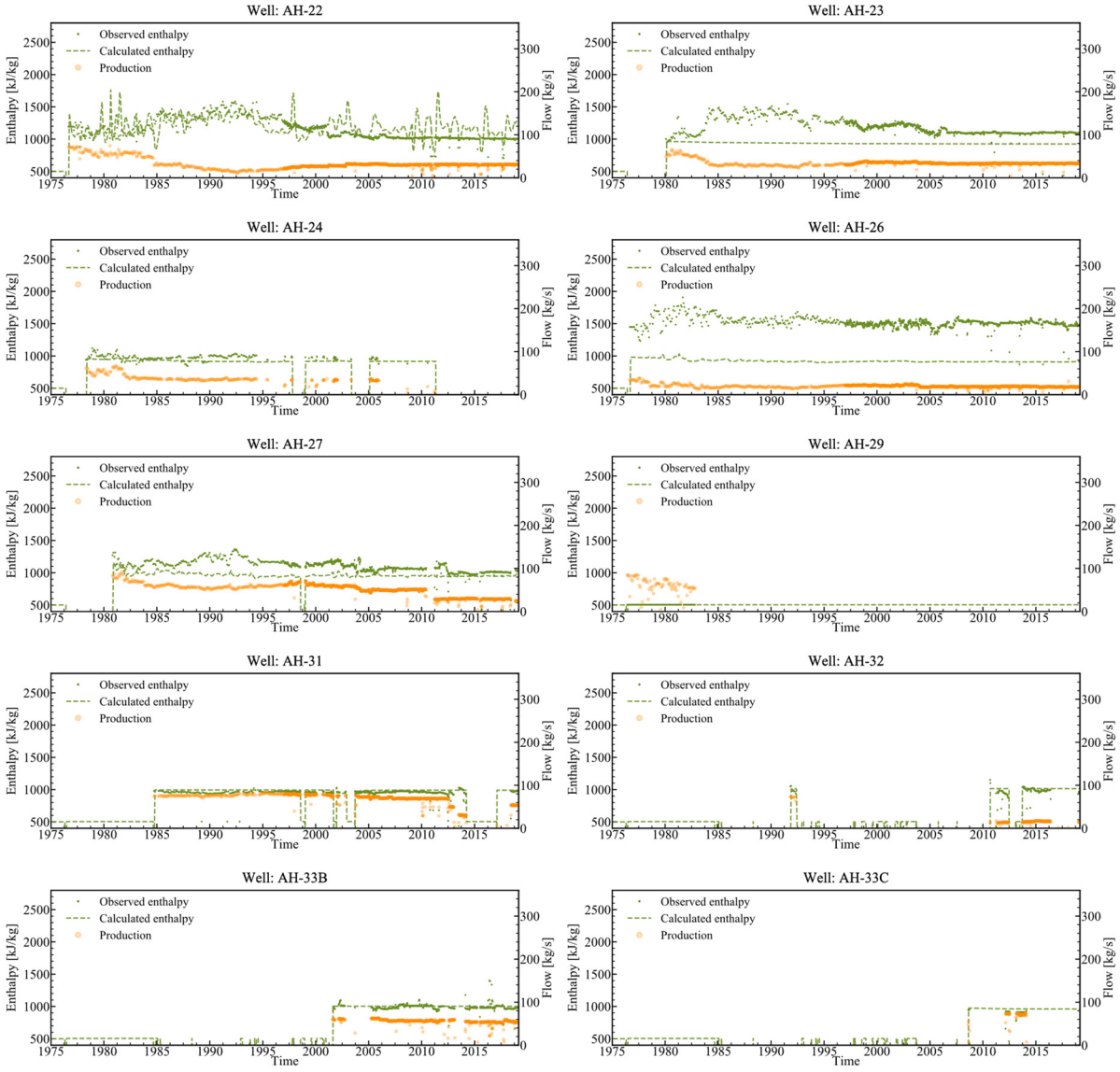
Well: AH-22
Well: AH-23
Well: AH-24
Well: AH-26
Well: AH-27
Well: AH-29
Well: AH-31
Well: AH-32
Well: AH-33B
Well: AH-33C
Observed enthalpy
Calculated enthalpy
Production
Enthalpy [kJ/kg]
Flow [kg/s]
Time

APPENDIX IV: Comparison between observed and calculated drawdown